Cell Systems

Article

G1/S Transcription Factor Copy Number Is a Growth-Dependent Determinant of Cell Cycle Commitment in Yeast

Graphical Abstract

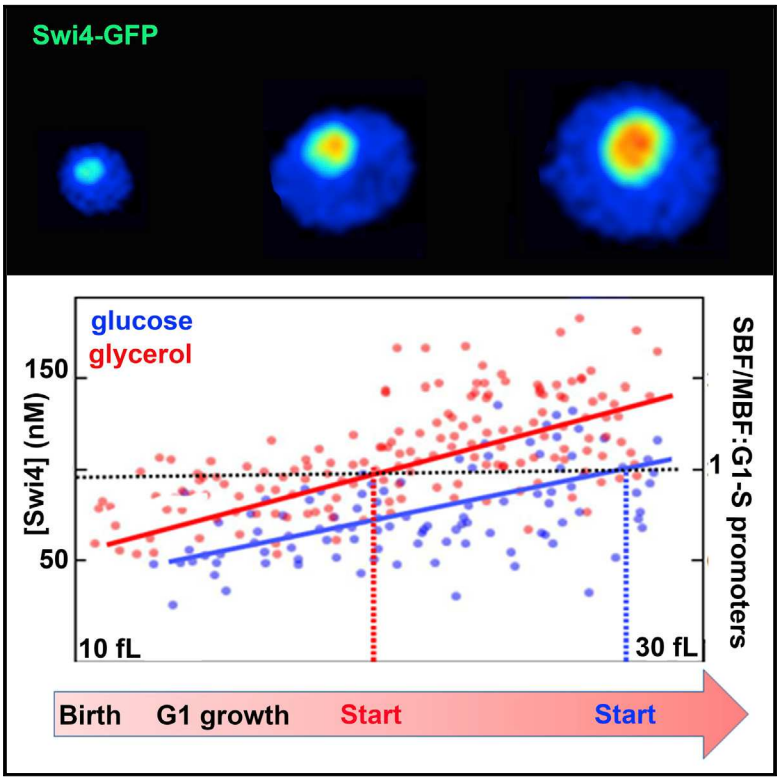

Highlights

- Absolute concentrations and stoichiometries of main G1/S regulators in live single cells
- G1/S transcription factors titrate a regulon of ~200 promoters as cells grow in G1 phase
- Transcription factor upregulation in poor nutrients saturates G1/S regulon at smaller size
- Mathematical model predicts growth and nutrient dependence of cell-cycle commitment

Authors

Savanna Dorsey, Sylvain Tollis, Jing Cheng, Labe Black, Stephen Notley, Mike Tyers, Catherine A. Royer

Correspondence

md.tyers@umontreal.ca (M.T.), royerc@rpi.edu (C.A.R.)

In Brief

Cell size results from a balance between growth and division and is central to proper control of proliferation of all cell types in all organisms. External signals - such as nutrients and growth factors - modulate cell size, and disruption of size control can lead to disease. While many genes implicated in size control have been identified, the underlying mechanisms that set size are poorly understood. Measurement of the absolute concentrations of the main G1/S transcription factors in budding yeast revealed that titration of target G1/S promoters occurs as cells grow and that saturation correlates with commitment to division at a critical size threshold in late G1 phase. Upregulation of the concentration of G1/S transcription factors under poor nutrients allows cells to reach the critical threshold at a smaller size.

Dorsey et al., 2018, Cell Systems 6, 539–554
May 23, 2018
https://doi.org/10.1016/j.cels.2018.04.012

CellPress

Cell Systems
Article

G1/S Transcription Factor Copy Number Is a Growth-Dependent Determinant of Cell Cycle Commitment in Yeast

Savanna Dorsey,[1,4] Sylvain Tollis,[2,3,4] Jing Cheng,[2] Labe Black,[1] Stephen Notley,[1] Mike Tyers,[2,*] and Catherine A. Royer[1,5,*]

[1]Department of Biological Sciences, Rensselaer Polytechnic Institute, Troy, NY 12180, USA
[2]Institute for Research in Immunology and Cancer, Université de Montréal, Montréal, QC H3T 1J4, Canada
[3]Wellcome Trust Centre for Cell Biology, Institute of Cell Biology, School of Biological Sciences, The University of Edinburgh, Edinburgh EH9 3JR, UK
[4]These authors contributed equally
[5]Lead Contact
*Correspondence: md.tyers@umontreal.ca (M.T.), royerc@rpi.edu (C.A.R.)
https://doi.org/10.1016/j.cels.2018.04.012

SUMMARY

To understand how commitment to cell division in late G1 phase (Start) is controlled by growth and nutrients in budding yeast, we determined the absolute concentrations of the G1/S transcription factors SBF (composed of Swi4 and Swi6) and MBF (composed of Mbp1 and Swi6), the transcriptional repressor Whi5, and the G1 cyclins, Cln1 and Cln2, in single live yeast cells using scanning number and brightness (sN&B) microscopy. In rich medium, Whi5, Mbp1, and Swi6 concentrations were independent of cell size, whereas Swi4 concentration doubled in G1 phase, leading to a size-dependent decrease in the Whi5/Swi4 ratio. In small cells, SBF and MBF copy numbers were insufficient to saturate target G1/S promoters, but this restriction diminished as cells grew in size. In poor medium, SBF and MBF subunits, as well as Cln1, were elevated, consistent with a smaller cell size at Start. A mathematical model constrained by sN&B data suggested that size- and nutrient-dependent occupancy of G1/S promoters by SBF/MBF helps set the cell size threshold for Start activation.

INTRODUCTION

Cell growth and division must be tightly coordinated to achieve a characteristic homeostatic cell size (Jorgensen and Tyers, 2004; Turner et al., 2012; Ginzberg et al., 2015; Wood and Nurse, 2015). In budding yeast, commitment to cell division occurs in late G1 phase, an event termed Start (Hartwell et al., 1974; Johnston et al., 1977). Prior to Start, G1 phase cells grow in order to accumulate energy reserves and build biosynthetic capacity necessary for the duplication of the genome and cellular biomass. Start occurs upon attainment of a critical cell size in late G1 phase (Figure 1A), at which point the cell initiates a complex G1/S transcriptional program of ~200 genes that encode proteins necessary for bud emergence, DNA replication, spindle body duplication, and other processes. The size threshold enforces a sufficiently long G1 phase to allow replication origins to be properly loaded, which is essential for S phase completion and genome stability (Lengronne and Schwob, 2002), and also helps establish a homeostatic size at the population level (Jorgensen et al., 2004).

Nutrient conditions and other environmental factors affect critical cell size. Budding yeast cells grown on rich nutrients such as glucose are substantially larger than those grown on poor carbon sources such as ethanol or glycerol. Pre-Start G1 phase cells grown on an optimal carbon source pass Start at a small size when shifted to a suboptimal source, whereas the converse shift delays Start until cells have attained a larger size (Johnston et al., 1977). In addition, nutrients also influence the extent of bud growth in mitosis and thereby the birth size of daughter cells (Leitao and Kellogg, 2017). This dynamic regulation of the size threshold by nutrients allows single-celled microorganisms to cope with the ever-changing environment, and thereby maximize competitive fitness (Jorgensen and Tyers, 2004). These observations frame two fundamental questions: (1) How does the Start machinery set a particular critical size threshold? (2) How is the threshold modulated by nutrient conditions?

The core network of proteins that executes Start has been identified and characterized (Figure 1B). The G1 cyclins Cln1, Cln2, and Cln3 are essential, rate-limiting activators of the cyclin-dependent kinase Cdc28 at Start. Cln-Cdc28 activity triggers G1/S transcription by directly stimulating two related heterodimeric transcription factor complexes called SBF (for Swi4/6 cell-cycle box binding factor) and MBF (for Mlu1 cell-cycle box binding factor), composed of the common activating subunit Swi6 and two related DNA binding subunits Swi4 and Mbp1, respectively (Koch et al., 1993). SBF and MBF can both recognize specific promoter motifs, termed SCB and MCB sites, that are present in most G1/S promoters (Koch et al., 1993; Iyer et al., 2001). Cells devoid of either Cln-Cdc28 activity or SBF/MBF arrest at Start (Richardson et al., 1989; Nasmyth and Dirick, 1991; Koch et al., 1993). In pre-Start

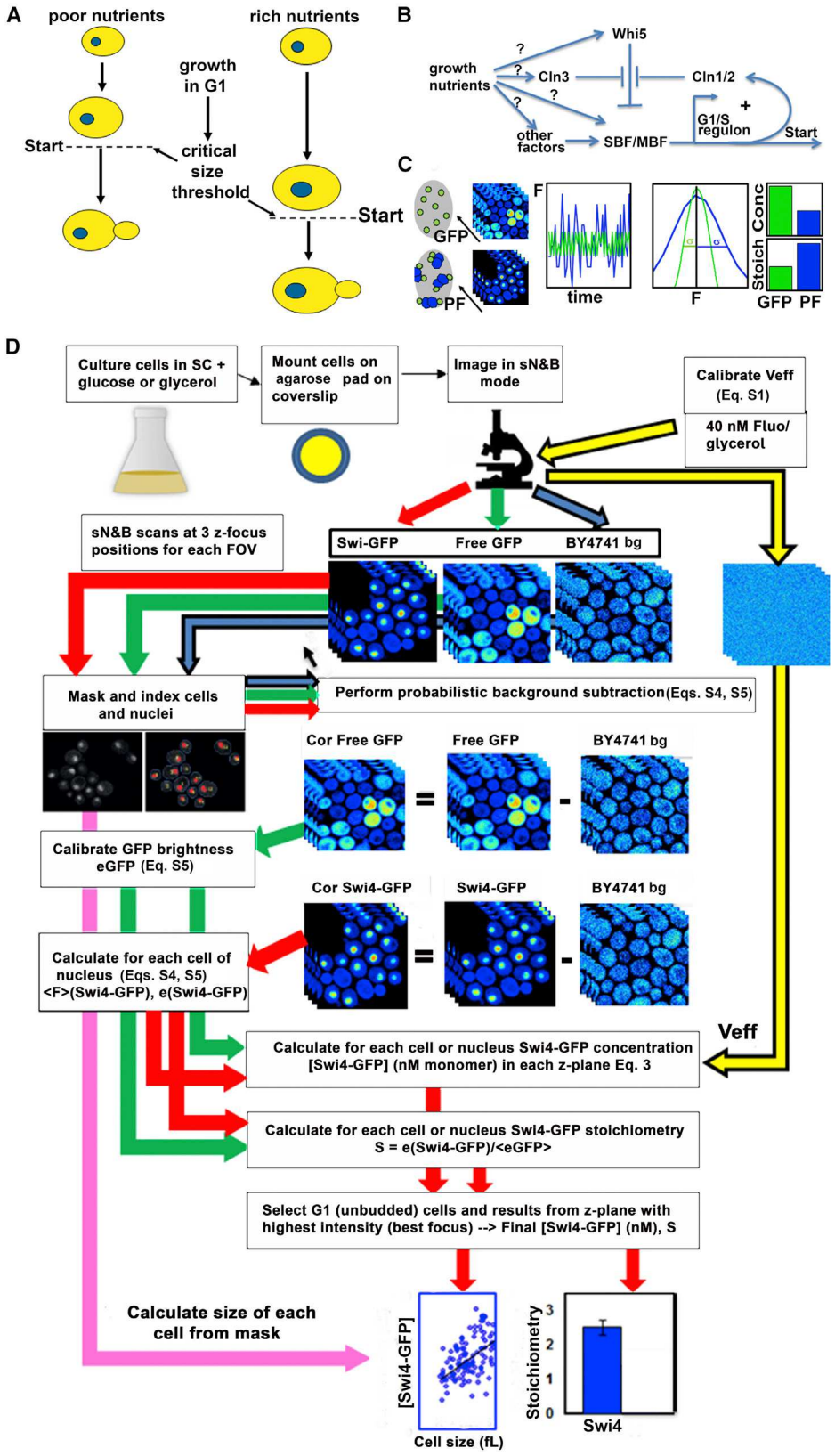

(legend on next page)

G1 cells, SBF is bound and held in check by a transcriptional repressor called Whi5 (Jorgensen et al., 2002; Costanzo et al., 2004; De Bruin et al., 2004). Phosphorylation of Whi5 and Swi6 on multiple sites by Cln-Cdc28 causes the dissociation of the complex and nuclear export of Whi5, which is thought to be the molecular event that defines Start (Costanzo et al., 2004; De Bruin et al., 2004; Wagner et al., 2009). SBF-Whi5 phosphorylation is initiated by Cln3, which peaks earlier in G1 phase and acts upstream of Cln1 and Cln2 (Tyers et al., 1993). *CLN1/2* themselves are critical early SBF target genes that form a positive feedback loop with SBF whereby Cln1/2 and SBF activity is rapidly co-amplified to effect irreversible activation of Start (Skotheim et al., 2008; Eser et al., 2011).

The core Start machinery is influenced by additional factors that modulate G1/S transcription. These regulators include the transcription factor, Bck2, which acts redundantly with the Cln3-SBF axis (Ferrezuelo et al., 2009), histone deacetylases associated with SBF/MBF (Huang et al., 2009; Wang et al., 2009), additional G1 cyclins that activate the Pho85 kinase (Huang et al., 2009), the MBF-specific repressor Nrm1 (de Bruin et al., 2006), the Whi5 ortholog Whi7 (Yahya et al., 2014), the quiescence-specific SBF repressors Msa1 and Msa2 (Miles et al., 2016), and daughter-cell-specific repressors of *CLN3* and *SWI4* transcription (Di Talia et al., 2009). Systematic genetic screens have revealed many hundreds of other genes that influence cell size (Jorgensen et al., 2002; Zhang et al., 2002; Dungrawala et al., 2012; Soifer and Barkai, 2014), but the genetic relationships of these factors with the Start machinery has yet to be established.

The conserved target of rapamycin (TOR) and protein kinase A (PKA) nutrient signaling networks stimulate growth rate and increase cell size (Jorgensen and Tyers, 2004). Activation of the PKA pathway by glucose represses *CLN1* and other G1/S transcripts, thereby helping to increase cell size in rich nutrients (Baroni et al., 1994; Tokiwa et al., 1994; Flick et al., 1998; Amigoni et al., 2015). The TORC1 complex controls many aspects of growth, including the rate of ribosome biogenesis, which has been linked to the size threshold (Jorgensen et al., 2002, 2004; Lempiäinen et al., 2009; Singh and Tyers, 2009). The phosphatase PP2A connects other upstream nutrient signals to cell size. In the absence of TORC1 activity, the Rim15 kinase inactivates the $PP2A^{Cdc55}$ isoform to enhance Whi5 phosphorylation (Talarek et al., 2017), while the $PP2A^{Rts1}$ isoform inhibits the TORC2 complex and ceramide biosynthesis to adjust cell size (Lucena et al., 2018). The rate of cell growth may be transmitted to the Start machinery by the action of the Ydj1 chaperone on Cln3 (Aldea et al., 2017). Metabolic cues, such as intracellular NAD+ concentration (Moretto et al., 2013), acetylation (Kaluarachchi Duffy et al., 2012), and intracellular pH (Dechant et al., 2014), also appear to modulate cell size.

Although the core Start machinery is well characterized genetically, the mechanisms whereby cell size is coupled to G1/S transcriptional activation remain enigmatic. Genetic dosage experiments demonstrate that a threshold level of Cln activity must be reached in order for cells to pass Start (Nash et al., 1988; Schneider et al., 2004), and that *SWI4* dosage is also limiting (McInerny et al., 1997). Notably, as extra plasmid-borne copies of SCB sites cause a Start delay, it has been posited that Cln3-Cdc28 activity may be titrated against G1/S promoter copy number (Wang et al., 2009). Most recently, it has been suggested that a fixed amount of Whi5 imparted to cells in early G1 phase serves as a metric that is gradually diluted as cells grow (Schmoller et al., 2015). However, earlier studies suggested that Whi5 does not change in concentration through the cell cycle (Costanzo et al., 2004; De Bruin et al., 2004). A particular further puzzle is that nutrients appear to govern the size threshold independently of the Cln3-Bck2-Whi5 axis (Costanzo et al., 2004).

Given the evident genetic complexity of the Start network, we sought to uncover the underlying behavior of the core G1/S machinery as a function of cell size and nutrient conditions. We used a particle-counting method called scanning number and brightness (sN&B) microscopy (Figure 1C) to measure absolute concentrations of GFP fusions of Swi4, Mbp1, Swi6, Whi5, Cln1, and Cln2 in single live yeast cells. We observed that the concentrations of Mbp1, Swi6, and Whi5 were independent of cell size in G1 phase, while in contrast Swi4 concentration increased as cells grew in size. These absolute values revealed that total SBF/MBF copy number was initially limiting with respect to target G1/S promoters in small cells but reached site saturation as cells approached Start, consistent with titration of G1/S promoters by SBF/MBF. Cln1 and MBF abundance, and to a lesser extent SBF, were markedly upregulated in glycerol compared with glucose

Figure 1. Cell Size, Start and Scanning Number, and Brightness Analysis

(A) Schematic representation of nutrient-dependent control of the G1 phase cell size threshold in budding yeast.

(B) Schematic representation of the main regulators of Start.

(C) General sN&B approach. Two different hypothetical samples are compared, free monomeric GFP and a dimeric GFP protein fusion (PF). In both cases there are on average eight molecules of GFP (in monomer units) in the excitation volume (gray oval), but the protein fusion is dimeric. Because there are twice as many GFP monomers in the dimer (blue trace) than for free GFP (green trace), the dimer fluctuations are twice as large. The concentration of the dimeric GFP fusion protein is half that of the free monomeric GFP because the stoichiometry is twice as large.

(D) Schematic diagram of the sN&B calibration, acquisition, and analysis workflow. Three yeast strains were analyzed in each experiment: the background parent strain BY4741 (blue arrows), BY4741 cells expressing free GFP (green arrows), and BY4741 cells expressing the protein of interest as a GFP fusion (Swi4 in this case, red arrows). To calibrate the V_{eff}, a solution of fluorescein of known concentration in 40% glycerol (yellow arrows) is used. The average free GFP and GFP protein fusion molecular brightness values for each cell or nucleus, e_{GFP}, and e_{PF}, are calculated using Equation 1. Then the absolute value of the GFP fusion concentration in each cell or nucleus is derived according to Equation 3. The ratio of the molecular brightness of the GFP protein fusion over that of free GFP yields the stoichiometry of the protein of interest. Optimal z position for focal plane is chosen to yield the final values of the concentration and stoichiometry in individual nucleus. Cell sizes for each cell are calculated from the results of the masking routine. Shown is an example of the concentration of Swi4-GFP in each cell versus cell size, and average Swi4-GFP stoichiometry.

Further details are provided in the STAR Methods and Supplemental Information.

medium, suggesting a simple molecular basis for acceleration of Start progression in poor nutrients. A minimal mathematical model of Start based on these quantitative measurements accurately predicted cell size on rich and poor media in different mutant backgrounds. Our results implicate titration of SBF/MBF copy number against G1/S promoters as a critical determinant of Start and provide a plausible explanation for how poor nutrients reduce critical cell size.

RESULTS

Determination of Absolute Protein Concentrations by sN&B in Live Yeast Cells

A quantitative understanding of Start requires accurate values for the absolute concentrations of the main Start regulators. However, the published copy number estimates for the various transcription factors and G1 cyclins vary by up to 60-fold (Table S1) (Cross et al., 2002; Ghaemmaghami et al., 2003; Kulak et al., 2014). To address this shortfall in quantitative parameterization, we used an image-based variation of particle-counting methods in fluctuation microscopy called sN&B (Magde et al., 1974; Digman et al., 2008).

Since its development in 2008, the sN&B approach has been used routinely to measure complex stoichiometries and protein concentrations in mammalian cell lines (Digman et al., 2013, and references therein) and in bacteria (Ferguson et al., 2011, 2012; Bourges et al., 2017). sN&B analysis uses the magnitude of the fluctuations in fluorescence, σ^2, relative to the average intensity, $\langle F \rangle$, obtained from a small optical observation volume, V_{eff}, to deconvolve the average intensity into the number of fluorescent particles in the volume, n, and their molecular brightness, e, measured as photon counts per acquisition time per particle ($\langle F \rangle = n \times e$) (Figure 1C). A small number of very bright particles gives rise to larger fluctuations than a large number of dim ones. sN&B entails the acquisition of multiple, rapid raster scans of the same field of view (FOV), thereby providing spatial maps of absolute number and brightness. For any given fluorescent protein fusion (PF), from the intensity average ($\langle F \rangle_{PF}$) and variance (σ^2_{PF}) at each pixel, the number of photon counts per dwell time associated with each PF (molecular brightness, e_{PF}) is determined as

$$e_{PF} = (\sigma^2_{PF} / \langle F \rangle_{PF}) - 1 \qquad \text{(Equation 1)}$$

The absolute number of PF (n_{PF}) in the V_{eff} at each pixel in the FOV can also be derived from the average and the variance in fluorescence intensity

$$n_{PF} = \langle F \rangle_{PF} / ((\sigma^2_{PF} / \langle F \rangle_{PF}) - 1) = \langle F \rangle_{PF} / e_{PF} \qquad \text{(Equation 2)}$$

However, to obtain more precise values for the absolute concentrations of GFP fusions of the main Start regulators in live yeast cells, we used average fluorescence, $\langle F \rangle_{PF}$, and two calibration parameters, the molecular brightness of monomeric GFP (GFPmut3, hereafter referred to as GFP for brevity) (Cormack et al., 1996), e_{GFP}, measured in live cells of the same genetic background concomitantly, and V_{eff}, determined using a solution of fluorescein of known concentration in 40% glycerol. Then, the absolute concentrations of the GFP fusion proteins in single nuclei, $[PF]_{nuc}$ (in units of monomeric GFP), were obtained by averaging their average fluorescence, $\langle F \rangle_{PF}$, over all pixels in each nucleus (or cytoplasm):

$$[PF]_{nuc}\,(M) = \langle F \rangle_{PF,nuc}\,(\text{counts} \cdot \tau^{-1}) / (e_{GFP}(\text{counts} \cdot \tau^{-1} \cdot \text{GFP monomer}^{-1}) \times V_{eff}(\text{l}) \times N_A\,(\text{molecules} \cdot \text{mol}^{-1})) \qquad \text{(Equation 3)}$$

Stoichiometries of the PFs were calculated from brightness as determined by Equation 1, relative to that of monomeric GFP, e_{PF}/e_{GFP}. A homodimeric complex therefore has twice the molecular brightness of monomeric GFP.

We applied the experimental sN&B workflow shown in Figure 1D to quantify the abundance and stoichiometry of the main Start regulators Swi4, Mbp1, Swi6, Whi5, Cln1, and Cln2. Both abundance and stoichiometry values are needed to define the ratios between each regulator and the target G1/S promoters. A detailed explanation of how protein concentrations and the associated uncertainties were determined by sN&B is provided in the Methods Details section of the STAR Methods and in the Supplemental Information. Benchmarking and control data can be found in Figures S1–S10. Each GFP fusion protein was integrated at the endogenous chromosomal locus and expressed from the native promoter (see Key Resources Table). Each of the GFP protein fusion strains used in this study exhibited a wild-type (WT) cell size distribution suggesting minimal interference with function (Figure S8).

Whi5 Concentration Is Invariant with Cell Size and Time

We first examined the levels of Whi5 since inactivation of Whi5 by phosphorylation is thought to be the molecular event that underpins cell-cycle commitment. To determine the behavior of Whi5 throughout G1 phase in WT yeast G1 cells, we studied unbudded pre-Start cells within an asynchronously growing population grown in synthetic complete (SC) medium with 2% glucose as a rich carbon source. The change in subcellular localization of Whi5 is an established molecular marker for Start (Costanzo et al., 2004; De Bruin et al., 2004): before Start, Whi5 is predominantly nuclear, whereas, after Start, Whi5 is predominantly cytoplasmic (Figure 2A). We used sN&B to quantify Whi5 concentration within a 2-min time window across an unperturbed asynchronous population of cells, and found that the nuclear Whi5 concentration in pre-Start cells was invariant with respect to cell size, ~120 nM on average, and concordantly, that total Whi5 copy number increased as cells grew in G1 phase (Figures 2B and 2C; Table 1). Whi5 concentration was much lower in the cytoplasm (~5 nM) than in the nucleus (~120 nM) in pre-Start cells, and this value was also size independent (Figure S11).

The observation that Whi5 concentration was independent of cell size contradicted a recent report that Whi5 is diluted as cells grow in G1 (Schmoller et al., 2015). To understand this discrepancy, we tested whether Whi5 concentration changed in individual cells over time by culturing cells in a microfluidics device and performing sN&B at 20-min intervals. To correct for photo-bleaching (Shaner, 2014; Ettinger and Wittmann, 2015), the intensity of free GFP expressed from a plasmid was measured at identical time points in a parallel microfluidics channel (Figure 3A). We observed a 3.7-fold decrease in the fluorescence intensity of free GFP over the time course of the experiment due to photo-bleaching. After

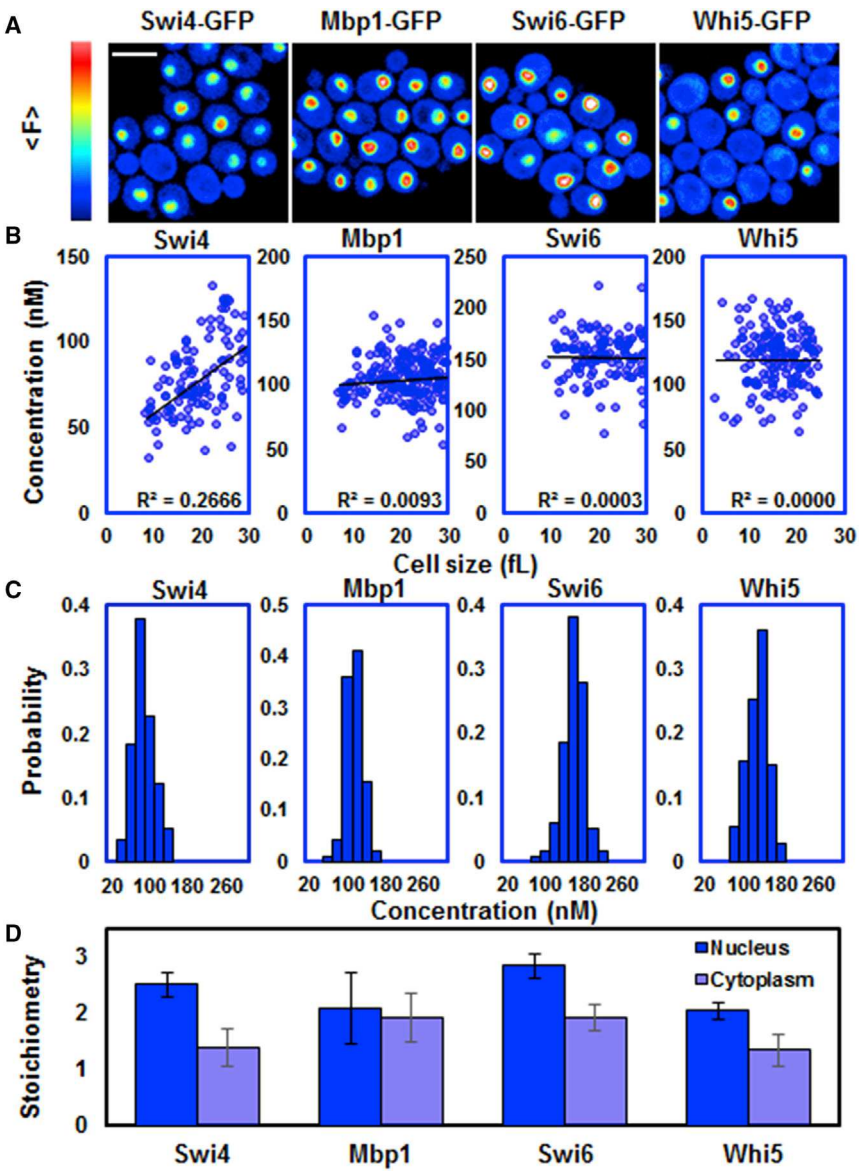

Figure 2. sN&B Quantification of Start Transcription Factors for G1 Phase Cells Grown on Glucose Medium

(A) Representative average fluorescence images of GFP fusions to each indicated protein. Full-scale intensity is 2.02 photon counts per 40-μs dwell time. Scale bar, 5 μm.

(B) Absolute concentrations in individual cell nuclei (each point is one nucleus) as a function of cell size for each indicated protein. Data are from at least three independent experiments performed on separate days. Total number of cells in each experiment were N = 114 (Swi4-GFP), 194 (Mbp1-GFP), 118 (Swi6-GFP), and 147 (Whi5-GFP). Scatter dot plots were linearly fitted to extract cell size dependence of protein concentrations. Pearson coefficients (R^2) are shown in the bottom right of each plot.

(C) Frequency histogram of single-cell data displayed in (B), reflecting the cell-to-cell biological variability in protein expression levels.

(D) Stoichiometries of GFP fusion proteins in the nucleus (dark blue bars) or the cytoplasm (light blue bars) extracted from brightness values averaged within each compartment. Bar height and error bars represent, respectively, the mean stoichiometries and SD over the populations of individual Swi4-GFP, Mbp1-GFP, Swi6-GFP, and Whi5-GFP cells analyzed to produce (B) and (C).

correction for this degree of GFP photo-bleaching, no time-dependent decrease in Whi5-GFP intensity was observed (Figures 3B and 3C). We also verified that Whi5 concentration was size independent in post-Start cells in both glucose and glycerol medium (Figures 3D and 3E), with the exception of a few very large cells in glucose. To rule out the possibility that cytoplasmic, rather than nuclear Whi5, was diluted over time in G1, we also quantified total Whi5 copy number in pre-Start (nuclear + cytoplasmic) versus post-Start (cytoplasmic) cells, and observed that the total amount of Whi5 increased monotonically with respect to cell size (Figure 3F). Moreover, the cell-averaged Whi5 concentration in post-Start cells was 6–7 times smaller than the pre-Start nuclear concentration, consistent with simple dilution of the nuclear Whi5 pool into the cytoplasmic compartment at Start (Jorgensen et al., 2007) (Figure S12). These observations were not specific to our microfluidics platform, to the sN&B approach, or strain background. We imaged thousands of asynchronously grown Whi5-GFP cells in either the BY4741 or W303 strain backgrounds in various media with an Opera high-content confocal microscope, using a single exposure to prevent photo-bleaching, and observed no correlation between Whi5 intensity and cell size (Figures 3G–3J). These independent approaches demonstrated that Whi5 continues to be synthesized and accumulates in total abundance as cells grow throughout G1 phase, and therefore that dilution of Whi5 cannot be a sensor for the increase in cell size. To probe other possible growth-dependent events that initiate Start, we turned our attention to the SBF and MBF transcription factors.

The Copy Number of SBF/MBF Subunits Correlates with Cell Size in G1 Phase

We carried out sN&B experiments with Mbp1-GFP, Swi6-GFP, and Swi4-GFP strains, using unbudded morphology to identify G1 phase cells for analysis (Figure 2A). Localization patterns were consistent with published data (Huh et al., 2003). sN&B calculations carried out for hundreds of unbudded G1 phase cells revealed that the nuclear concentrations of Mbp1 and Swi6 were, on average, ~105 and 150 nM (monomer units), respectively, and were independent of cell size (Figures 2B and 2C; Table 1). Hence, as for Whi5, copy numbers for Mbp1 and Swi6 were 3-fold higher in the nuclei of large cells (248 and 339 molecules, respectively, for Mbp1 and Swi6) compared with small cells (79 and 113 molecules, respectively) (Table 1). The nuclear Swi4 concentration in small G1 phase cells, ~50 nM, was

Table 1. Average Concentrations, Copy Numbers, and Stoichiometries of G1/S Transcription Factors as a Function of Nuclear Size and Carbon Source as Determined by sN&B

	Small nuclei (1.25 fL)[a]		Large nuclei (3.75 fL)[a]	
Glucose				
Monomer units	Concentration (nM)	Copy number	Concentration (nM)	Copy number
Swi4	50	38	100	226
Mbp1	105	79	110	248
Swi6	150	113	150	339
Whi5	120	90	120	271
Copy-number ratio				
Swi4/Mbp1	N/A	0.48	N/A	0.91
Swi6/(Swi4 + Mbp1)	N/A	0.97	N/A	0.72
Whi5/Swi4	N/A	2.40	N/A	1.20
Whi5/Swi6	N/A	0.80	N/A	0.80
Swi4 dimers/ promoter DNA (200)	N/A	0.10	N/A	0.57
Mbp1 dimers/ promoter DNA (200)	N/A	0.20	N/A	0.62
(Mbp1 + Swi4) dimers/promoter DNA (200)	N/A	0.29	N/A	1.19
Glycerol				
Monomer units	Concentration (nM)	Copy number	Concentration (nM)	Copy number
Swi4	75	56	130	294
Mbp1	145	109	150	339
Swi6	185	139	200	452
Whi5	125	94	115	260
Copy-number ratio				
Swi4/Mbp1	N/A	0.51	N/A	0.87
Swi6/(Swi4 + Mbp1)	N/A	0.84	N/A	0.71
Whi5/Swi4	N/A	1.68	N/A	0.88
Whi5/Swi6	N/A	0.68	N/A	0.58
Swi4 dimers/ promoter DNA (200)	N/A	0.14	N/A	0.74
Mbp1 dimers/ promoter DNA (200)	N/A	0.27	N/A	0.85
(Mbp1 + Swi4) dimers/promoter DNA (200)	N/A	0.41	N/A	1.58

[a]Nuclear volume was calculated as 1/8 of total cell volume, which corresponds to a 7-fold difference between nuclear and cytosolic volume (Jorgensen et al., 2007). Small cell volume was 10 fL and large cell volume was 30 fL.

substantially lower than that of Mbp1 and Swi6, but doubled with cell size (Figures 2B and 2C), corresponding to a 6-fold increase in Swi4 copy number throughout G1 phase. This result at the protein level reflected previously reported 2- to 3-fold increases in *SWI4* mRNA at the population level during G1 phase progression (Silljé et al., 1997; MacKay et al., 2001), as well as an increase in Swi4 protein levels through G1 phase as determined by western blot (Harris et al., 2013). The cytosolic concentrations of Mbp1, Swi6, and Swi4 ranged between 10- and 75-fold lower than the nuclear concentrations (Figures S11A and S11B).

An advantage of sN&B over conventional fluorescence microscopy techniques is that observed intensity fluctuations scale linearly with the oligomeric state of a GFP-tagged protein (Equation 1). In the nucleus, the stoichiometries of Swi4, Mbp1, Swi6, and Whi5 were slightly larger than 2 (Figure 2D), suggesting that each protein exists predominantly as a homodimer with some formation of higher order oligomers. In contrast, all factors exhibited somewhat lower stoichiometry in the cytoplasm, likely because the lower concentrations favor dimer dissociation.

The total nuclear and cytosolic copy numbers for Swi4 and Mbp1 in G1 phase cells obtained from the sN&B analyses (Table S1) were in good agreement with those measured by mass spectrometry (Kulak et al., 2014), and 2- to 3-fold lower than those obtained by semi-quantitative western blot detection of tandem affinity purification-tagged proteins (Ghaemmaghami et al., 2003). A previous report determined the concentration of Mbp1 in rich medium by fluorescence correlation spectroscopy to be 60 nM, nearly identical to the value reported here once dimer formation is taken into account (Larson et al., 2011). For Swi6 levels, we observed reasonable agreement (~2-fold difference) with a previous determination of endogenous protein levels by mass spectrometry (Kulak et al., 2014), but a 10-fold lower level than determined by western blot analysis (Ghaemmaghami et al., 2003). The values for Whi5 determined by sN&B were intermediate between those previously reported, which themselves differed by a factor of 60 (Ghaemmaghami et al., 2003; Kulak et al., 2014). The cell-to-cell variability in nuclear protein levels in each sN&B experiment, as quantified by coefficients of variation, was ~20%, or about ~3-fold larger than the 7.5% maximal measurement-based variability (see the STAR Methods and Supplemental Information for details), implying substantial biological variability in SBF/MBF concentrations.

Assuming a size-independent nuclear-to-cytoplasmic ratio of 1:7 (Jorgensen et al., 2007), and using a small cell size of 10 fL (1.25 fL nucleus) and a large cell size of 30 fL (3.75 fL nucleus), we compared the size dependence of nuclear copy numbers for each protein (Figure 4A, Table 1). Nuclear Swi6 copy number was slightly lower than the total nuclear Mbp1 and Swi4 for all cell sizes, indicating that Mbp1 and Swi4 must compete for Swi6 throughout G1. Since full repression of SBF requires a stoichiometric excess of unphosphorylated Whi5 to saturate total SBF, an important parameter is the copy-number ratio of Whi5 to Swi4. Whi5 copy number was more than double that of Swi4 in small cells but, due to the increase in Swi4 concentration with size, this ratio decreased to ~1.1 in large cells (Figure 4C). This gradual reduction in the Whi5:Swi4 ratio arises from the observed increase in Swi4 concentration, not a decrease in Whi5 concentration, and combines with the phosphorylation-dependent reduction in Whi5-SBF affinity to activate Start (see below).

Activation of the ~200 genes in the G1/S regulon at Start also requires sufficient SBF or MBF to bind to one or more of the MCB or SCB target sites present in their promoter regions (Iyer et al.,

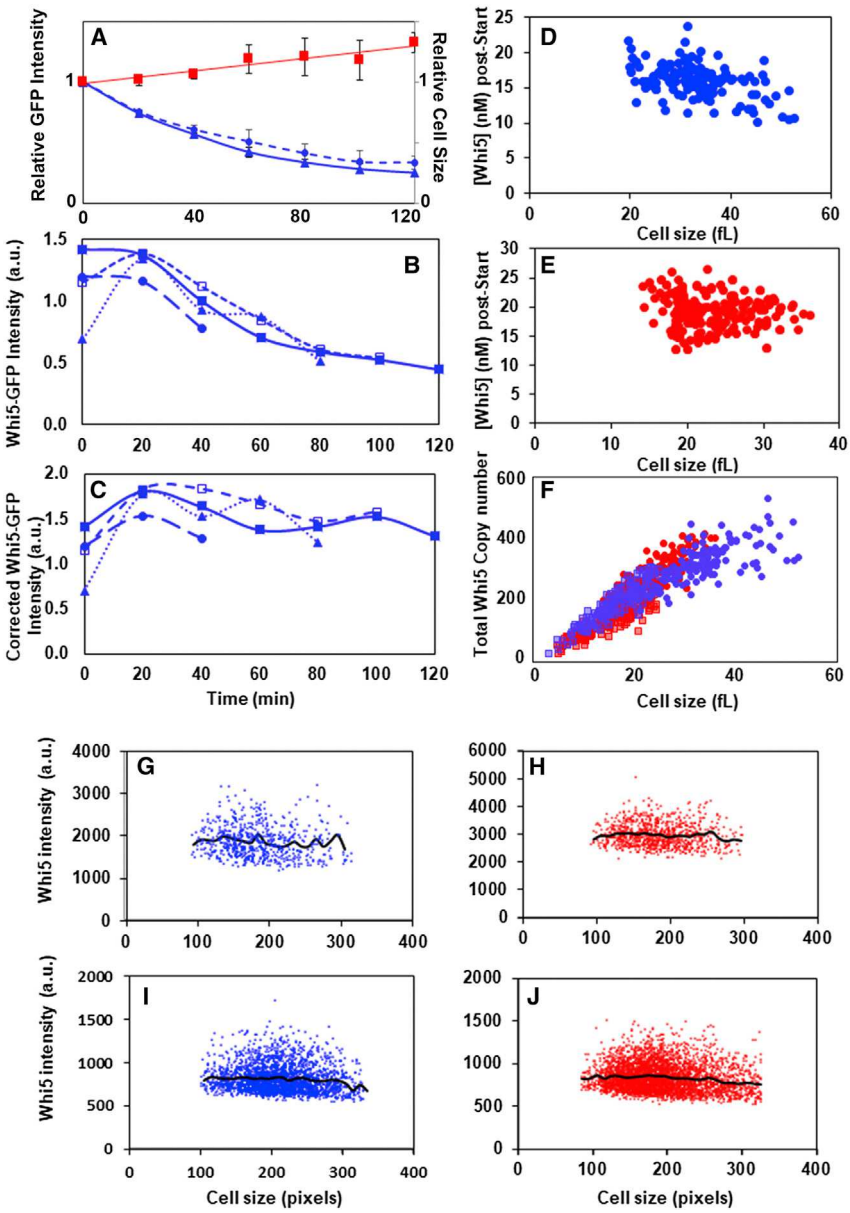

Figure 3. Whi5 Concentration Is Constant throughout G1 Phase

(A–C) Quantification of Whi5 in single cells by sN&B in a microfluidic device. (A) Time course of free GFP fluorescence intensity normalized to the initial intensity (blue triangles, blue line; average of three individual G1 cells expressing free GFP; see the STAR Methods for details). Individual cell sizes normalized to the initial sizes were scored at each time point and fitted to a linear growth curve (red squares, red line, points are averages of three individual cells; error bars are standard deviation of the average of three individual cells). These points were used to deconvolve the effect of cell volume expansion (GFP dilution) on GFP signal decrease, yielding the signal loss attributable to photobleaching only (blue circles, dashed blue line, average and standard deviation from three individual cells). Only the most slowly growing cells were monitored in order to obtain the longest possible time courses. a.u., arbitrary units.

(B) Normalized nuclear fluorescence intensity time courses from four individual G1 cells expressing Whi5-GFP and grown in SC + 2% glucose medium, acquired at the same time as samples in (A) in a parallel microfluidics channel. Since Whi5 is exported from the nucleus at Start, the individual time courses for each of these four cells ended when the cells passed Start.

(C) Whi5-GFP intensity time courses for the four cells in (B) corrected for the fraction of intensity loss attributable to photo-bleaching in (A).

(D–F) Quantification of Whi5 in pre-Start and post-Start cells by sN&B. Whi5-GFP concentration in post-Start cells in SC + 2% glucose (D) and SC + 2% glycerol (E) as a function of cell size. Since the cells were post-Start, Whi5-GFP was not present in the nucleus and concentrations are reported only for the cytoplasm. (F) Total Whi5 copy number in pre-Start (squares) and post-Start (circles) cells grown in SC + 2% glucose (blue) and SC + 2% glycerol (red). For each pre-Start cell, the total copy number was determined as the product of the concentration and the volume for the nuclear or cytoplasmic compartments (1/8 and 7/8 cell volume; Jorgensen et al., 2007).

(G–J) Quantification of Whi5 in a single image of asynchronous populations in different strain backgrounds. Nuclear Whi5-GFP fluorescence intensity versus cell size from single exposure obtained on an Opera high-content confocal microscope for individual G1 phase Whi5-GFP cells in the BY4741 background grown and imaged in (G) SC + 2% glucose (627 cells) or (H) SC + 3% glycerol + 3% ethanol (943 cells), and G1 phase Whi5-GFP cells in the W303 background grown and imaged in (I) SC + 2% glucose (2,445 cells) or (J) SC + 2% glycerol + 1% ethanol (4,127 cells). The solid lines represent the Whi5-GFP signal averaged over all cells of similar size for a bin width of 10 pixels.

2001; Di Talia et al., 2009; Ferrezuelo et al., 2010). Hence, we compared the cell size-dependent total dimeric copy number of Swi4 and Mbp1 with the number of their target promoters. In small G1 cells, the sum of the number of Swi4 and Mbp1 dimers in the nucleus (~120 total nomoers divided by two = ~60 copies) was less than one-third the number of G1/S promoters, whereas in large cells Swi4 and Mbp1 dimers summed up to ~240 copies, larger than the number of G1/S promoters (Figure 4D; Table 1). These results suggested that SBF/MBF are stoichiometrically limiting in newly born daughter cells, and that this limitation diminishes as cells progress through G1.

SBF and MBF Concentrations Are Upregulated in Glycerol Medium

While it has long been known that nutrients dynamically alter the critical cell size threshold (Johnston et al., 1979; Lorincz and Carter, 1979; Jorgensen et al., 2004), the manner in which these signals influence the G1/S transcriptional machinery is still largely unknown. We therefore carried out sN&B experiments in SC medium with 2% glycerol as the sole carbon source (Figures 4E and S11), in which cells have a mode size of 20–25 fL, i.e., at least 10 fL smaller than in glucose (Figure S8). Cells grew slowly in SC + 2% glycerol, but did not grow at all in SC

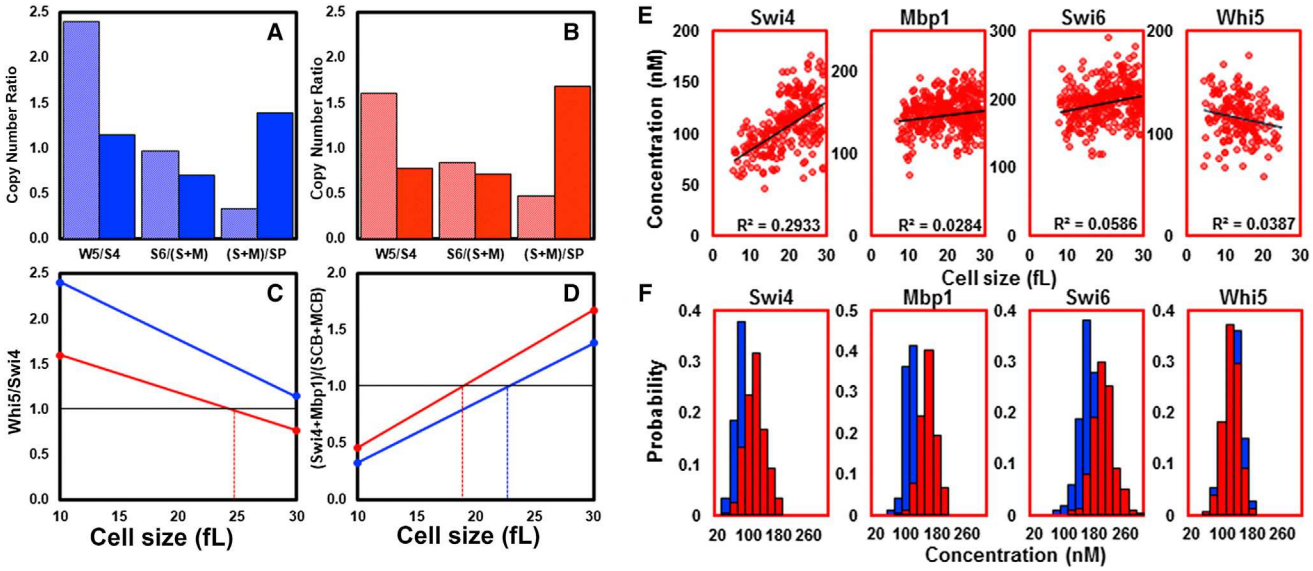

Figure 4. G1/S Transcription Factor Copy Numbers Change with Growth in G1 Phase and Are Upregulated in Glycerol

(A and B) Copy-number ratios for Whi5:Swi4, Swi6:(Mbp1+Swi4), and (Mbp1+Swi4 dimer units):(G1/S promoters) in cells grown in (A) SC + 2% glucose medium (small cells [blue stipple, 10 fL] and large cells [dark blue, 30 fL]) and (B) SC + 2% glycerol medium (small cells [red stipple, 10 fL] and large cells [dark red, 30 fL]). In both (A) and (B), protein concentrations were extracted from the linear fit of single-cell sN&B results in Figures 2B and 4E, and converted to copy number using a nuclear volume of 1/8 of total cell volume (Jorgensen et al., 2007).

(C and D) Change in average (C) Whi5:Swi4 copy-number ratio and (D) (Swi4 dimer + Mbp1 dimer):(G1/S promoters) ratio with size in cells grown in glucose (blue) versus glycerol (red) medium. Horizontal solid line indicates a ratio of 1, which is reached at a smaller size in glycerol than in glucose medium.

(E) Absolute nuclear concentrations for Swi4, Mbp1, Swi6, and Whi5 in SC + 2% glycerol medium. Data shown come from at least three independent experiments performed on separate days. Total number of cells in each experiment were N = 244 (Swi4-GFP), 342 (Mbp1-GFP), 324 (Swi6-GFP), and 211 (Whi5-GFP). Scatter dot plots were linearly fitted to extract cell size dependence of protein concentrations. Pearson coefficients (R^2) are shown in the bottom right of each plot.

(F) Frequency histogram representation of the single-cell data displayed in (E), reflecting the cell-to-cell variability in protein expression levels for cells grown in glycerol (red) versus cells grown in glucose (blue, data from Figure 2C) medium.

that lacked a carbon source (Figure S13). The concentrations of all SBF/MBF subunits, particularly for Mbp1, were higher in glycerol compared with glucose medium, whereas the concentration of Whi5 was not affected by carbon source (Figures 4E and 4F). This increase in concentration was not a consequence of a general increase in cellular protein content, which was similar in cells grown on glucose versus glycerol medium (Figure S14). As in glucose, Swi4 concentration showed a positive correlation with cell size in glycerol, whereas Mbp1, Swi6, and Whi5 concentrations remained constant with respect to cell size (Figure 4E). In addition, the stoichiometry of all SBF components in the nucleus in glycerol medium remained dimeric (Figure S11D). Because Swi4 was upregulated in glycerol medium both in small and large cells, whereas Whi5 was not, the Whi5:Swi4 ratio was lower for cells of all sizes in the poor carbon source compared with cells grown in glucose (Figures 4B and 4C). Moreover, due to the upregulation of all SBF and MBF subunits in glycerol, these factors were much less limiting with respect to promoter number in the G1/S regulon on the poor carbon source (Figures 4B and 4D). Both the lower Whi5:Swi4 ratio and a higher SBF + MBF:G1/S promoter ratio would be predicted to trigger Start at a smaller size in glycerol medium, as observed.

The more pronounced increase in Mbp1 concentration compared to Swi4 in glycerol medium suggested a potentially more prominent role for MBF in reducing the size threshold in poor carbon sources. Previously it has been shown that *CLN1* is repressed upon a shift from glycerol to glucose medium, and, correspondingly, that *cln1Δ* strains have a large size phenotype compared with WT on poor carbon sources (Tokiwa et al., 1994; Flick et al., 1998). The *CLN1* promoter contains three closely spaced MCB sites that bind SBF, confer G1/S transcription, and mediate glucose repression in a *SWI4*-dependent manner (Partridge et al., 1997; Flick et al., 1998; Amigoni et al., 2015). However, it is not known whether MBF contributes to the expression of *CLN1* in poor media. We measured the cell size distributions of WT, *cln1Δ, cln2Δ*, and *mbp1Δ* strains in glucose and glycerol medium (the very large size of *swi4Δ* cells precluded a meaningful comparison). As expected, the *cln1Δ* strain exhibited a glycerol-specific large phenotype, whereas the *cln2Δ* strain exhibited a large phenotype on both glucose and glycerol medium (Figure 5A). We observed only a subtle size increase for the *mbp1Δ* strain in glucose medium, in agreement with previous reports (Flick et al., 1998; Bean et al., 2005; Adames et al., 2015). In glycerol medium, *mbp1Δ* cells exhibited a large size phenotype when compared with the WT control (Figure 5A). It has been also reported that an *mbp1Δ cln3Δ* double mutant strain has a larger size on poor compared to rich carbon sources (Adames et al., 2015). These data support the notion that the ~50% increase in Mbp1 levels in WT cells grown in glycerol contributes to the smaller size at Start observed in this growth medium (Figures S3D–S3H). Collectively, these results indicated that increased abundance of SBF/MBF in glycerol

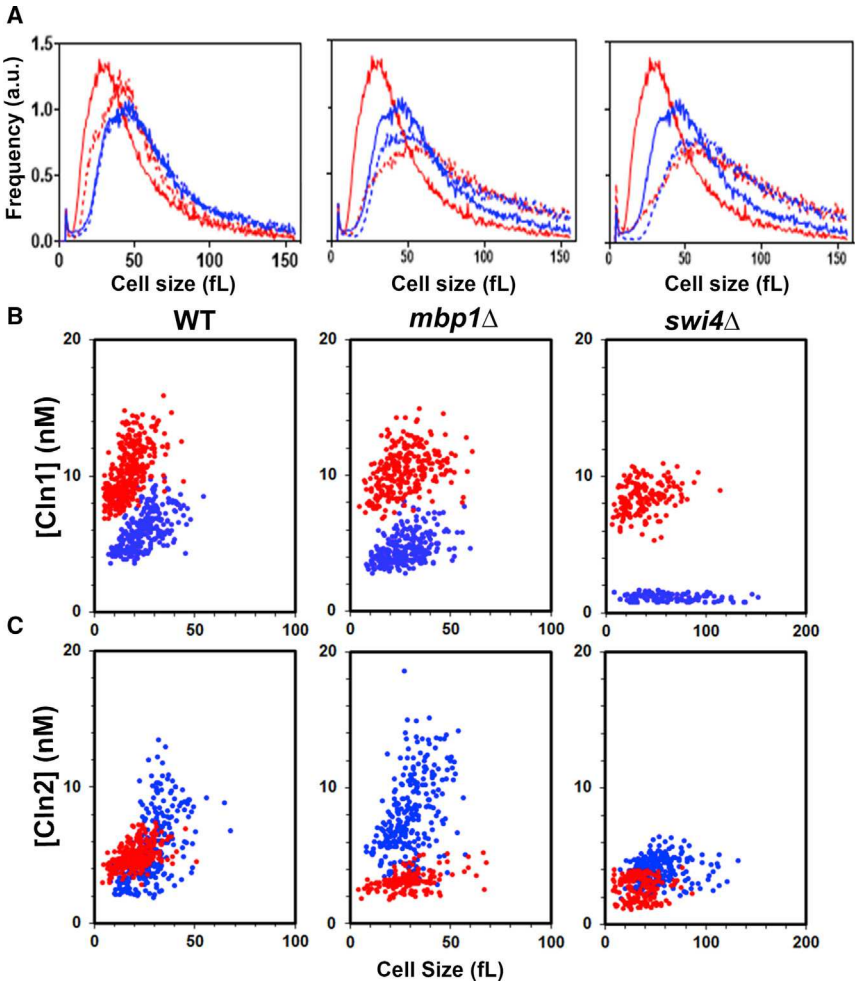

Figure 5. Nutrient-Dependent Size Phenotypes Correlate with MBF/SBF-Dependent Cln1/2 Expression Levels

(A) Coulter counter size distributions for WT and *mbp1Δ* deletion strains (left), WT and *cln1Δ* strains (center), and *cln2Δ* strains (right). Solid lines correspond to WT and dotted lines to the deletion strains in either SC + 2% glucose (blue) or SC + 3% glycerol (red) medium.

(B) Scatterplots of cell-averaged sN&B values for Cln1 concentration versus cell size in individual cells in an asynchronously grown culture in SC + glucose (blue) or SC + glycerol (red) medium for WT (left), *mbp1Δ* (middle), and *swi4Δ* (right) strains. Cells from all stages of the cell cycle are represented. Data are from at least three independent experiments performed on separate days (N = 263, 348, and 122, respectively, for WT, *mbp1Δ*, and *swi4Δ* in glucose; N = 522, 276, and 275 for the same strains in glycerol). Cells that could not be background-corrected were removed (N = 18, 16, and 53, respectively, for WT, *mbp1Δ*, and *swi4Δ* in glucose; N = 1, 3, and 2 for the same strains in glycerol).

(C) Scatterplots of cell-averaged sN&B values for Cln2 concentration versus cell size in individual cells in an asynchronously grown culture in SC + glucose (blue) and SC + glycerol (red) medium for WT (left), *mbp1Δ* (middle), and *swi4Δ* (right) strains. Each data point was obtained as above. Data are from at least three independent experiments performed on separate days (N = 299, 262, and 172, respectively, for WT, *mbp1Δ*, and *swi4Δ* in glucose; N = 223, 195, and 226 for the same strains in glycerol). Cells that could not be background-corrected were removed (N = 15, 23, and 14, respectively, for WT, *mbp1Δ*, and *swi4Δ* in glucose; N = 40, 29, and 44 for the same strains in glycerol).

medium reduces the size threshold, and that MBF plays a more prominent role under nutrient-limited conditions.

Nutrients Modulate SBF/MBF-Dependent Dynamics of Cln1/2 Accumulation

Given the differential genetic effects of *CLN1* and *CLN2* on size in different carbon sources, we quantified the levels of Cln1 and Cln2 proteins in glucose and glycerol in single live cells at all stages of the cell cycle in asynchronous cultures (Figures 5B, 5C, S15, and S16). We note that we were unable to reliably quantify levels of endogenously expressed Cln3 above background in asynchronous cells and therefore were unable to evaluate the response of Cln3 to growth and nutrient signals. Very few cells exhibited nuclear Cln1 or Cln2, indicating that these proteins were only transiently enriched in the nucleus in our experiments. Both Cln1 and Cln2 were monomers in the nuclear and cytoplasmic compartments (Figure S15). The average Cln1 concentration was ~5 nM in small WT cells grown in glucose and increased linearly with cell size. The Cln2 concentration was ~2 nM in small WT, glucose-grown cells, but increased non-linearly to ~12 nM in large cells, consistent with positive feedback amplification in glucose medium (Skotheim et al., 2008). The concentrations of Cln1 in glucose determined by sN&B were lower by a factor of 3- to 4-fold than those reported previously, while the Cln2 concentration we observed was 10- to 13-fold lower than previous estimates (Cross et al., 2002; Ghaemmaghami et al., 2003) (Table S1). Cln1/2 levels in all small G1 cells were well above the detection limit of ~1 nM, reflecting a low basal level of Cln1/2 expression even in early G1 phase cells. We note that, due to the ~6 min maturation time of GFPmut3 (Megerle et al., 2008) and the short 10 min half-life of Cln1/2 protein (Schneider et al., 1998, 2004), the concentrations derived from sN&B analysis of GFP fusion proteins could be under-estimated by ~40%. This correction yielded a value that is only 2-fold lower than that obtained previously for Cln1, but was insufficient to account for the considerably higher levels reported for Cln2 (Cross et al., 2002; Ghaemmaghami et al., 2003).

In glycerol medium, Cln1 levels were ~2-fold higher and accumulated more sharply with size compared with glucose-grown cells. Small WT cells grown in glycerol showed slightly higher average Cln2 concentrations in glycerol compared with glucose, but the amplification as cells grew was not as sharp. These single-cell quantification results suggested that Cln1/2 levels were elevated in poor nutrients, in contrast to previous western blot analyses that suggested substantially lower Cln1/2 levels on poor carbon sources (Schneider et al., 2004). We note that

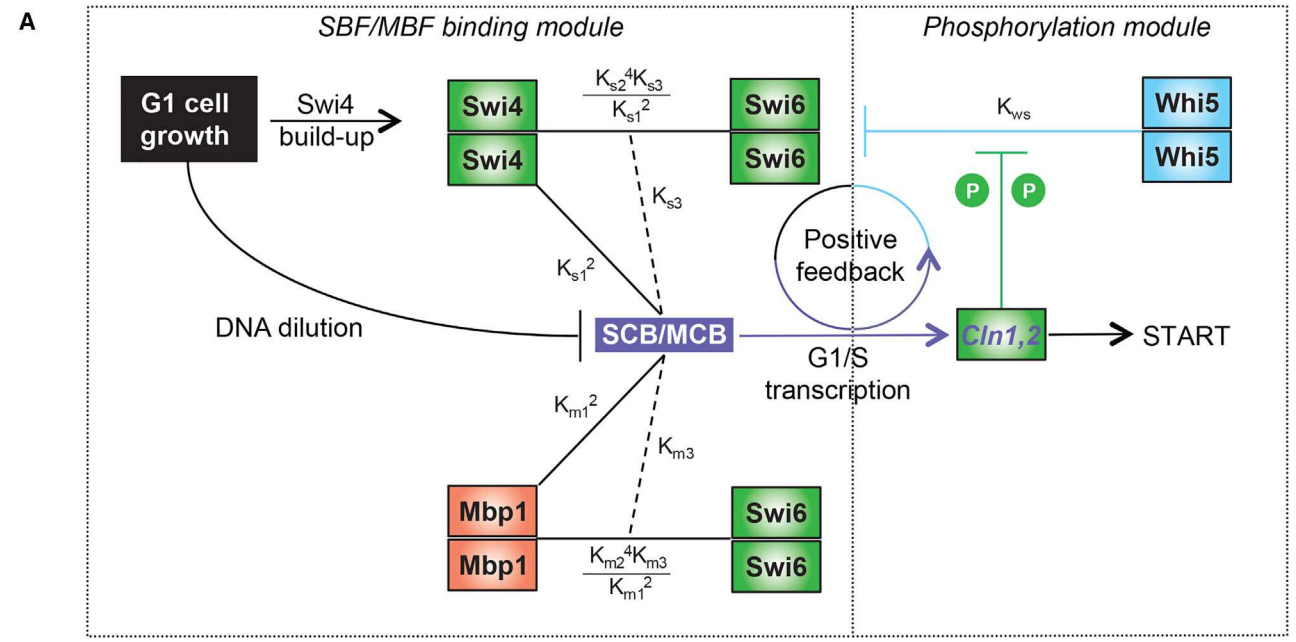

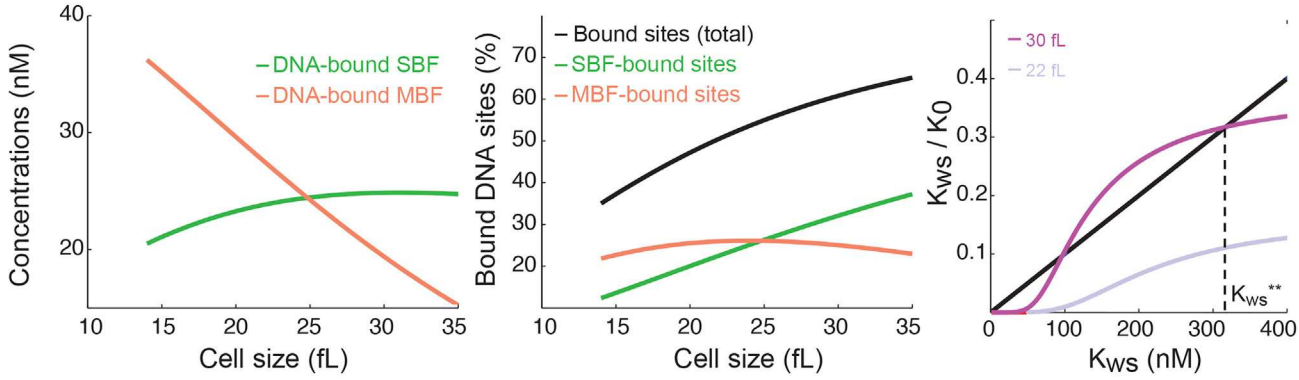

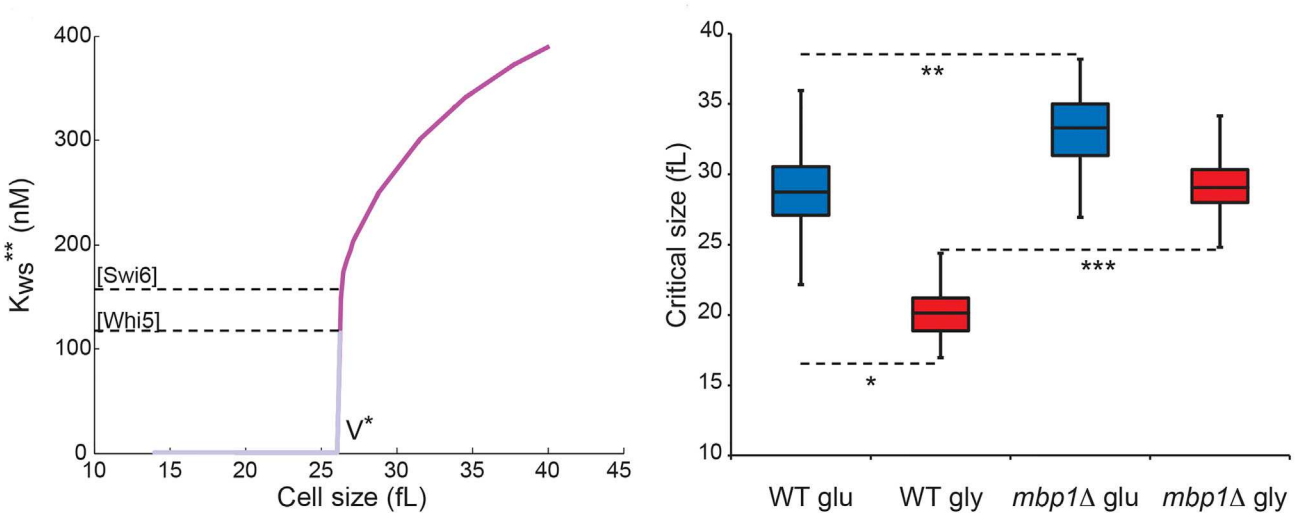

(legend on next page)

differences in intracellular pH that might affect the spectral properties of GFP under different nutrient conditions cannot account for this discrepancy. In poor nutrients, intracellular pH is lower than in glucose (Dechant et al., 2014), which, if anything, would quench GFP fluorescence, and yet we detect significantly higher Cln1/2 levels in glycerol medium. The much longer residence time of glycerol-grown cells in early G1 phase when Cln1/2 are present at low levels could also reduce the total population-averaged signal; however, this effect was controlled for by cell synchronization in previous studies (Schneider et al., 2004). The apparent difference in Cln1/2 abundance may be due to the non-linearity of antibody-based detection of proteins in cell extracts and/or potential inefficient protein extraction from small slow growing cells, but this remains to be ascertained in direct methodological comparisons. Taken together, the conditional large phenotype of the *cln1Δ* mutant and Cln1 upregulation in glycerol were consistent with a more prominent role for Cln1 in Start initiation on poor carbon sources.

We then asked how each component of SBF and MBF affected Cln1/2 levels. Deletion of *MBP1* had little effect on Cln1 or Cln2 concentrations in glucose medium, in agreement with the minimal effect on cell size (Figures 5B and 5C). In contrast, deletion of *SWI4* almost completely abrogated the Cln1 signal (down to the detection limit of ~1 nM), consistent with the known dominant contribution of SBF to *CLN1* expression in glucose. This much lower Cln1 level in the *swi4Δ* strain also suggested that the basal levels of *CLN1* expression in WT cells (5 nM) may be due to transcriptional bursting during transient Whi5 dissociation from SBF. Low-level expression from strongly repressed promoters in bacteria has also been detected by sN&B (Ferguson et al., 2012). The amplification of Cln2 expression depended heavily on *SWI4*, such that the peak concentration in large cells was reduced ~3-fold in the *swi4Δ* strain, while the basal concentration in small cells was almost unchanged. This strong dependence of Cln2 protein concentrations on Swi4 mirrored the quantitative decrease in *CLN2* promoter expression observed in a *swi4Δ* mutant (Bean et al., 2006).

In glycerol medium, neither *MBP1* nor *SWI4* deletion had much effect on Cln1 concentration, although the rate of Cln1 increase was dampened in both cases. These results indicated that MBF can effectively compensate for SBF in driving *CLN1* expression on poor carbon sources. The Cln2 concentration in glycerol medium was slightly lower than for WT cells in both *mbp1Δ* and *swi4Δ* cells. Thus, as in the case of *CLN1*, both MBF and SBF appeared to contribute to the modest linear increase of Cln2 in glycerol medium. Collectively, these results show that, in glycerol medium, the Cln1 concentration is elevated, positive feedback is less pronounced, and Mbp1 contributes prominently to *CLN1/2* expression, consistent with the relatively large size of *mbp1Δ* and *cln1Δ* cells in glycerol.

A Mathematical Model for Start Predicts Cell Size under Different Conditions

To evaluate whether the progressive saturation of G1/S promoters by SBF/MBF and the decrease in Whi5:Swi4 abundance ratio with increasing cell size constitute a plausible trigger for Start, we developed a mathematical model of a simplified Start network and constrained the model with sN&B data. The model encompassed interactions between the individual subunits of SBF/MBF complexes, their binding to target SCB/MCB sequences on DNA, and SBF inhibition by Whi5. Termination of SBF repression upon Whi5 dissociation and Whi5 exit from the nucleus was used as a proxy for Start (Costanzo et al., 2004; Bean et al., 2006). The interactions of Swi4/Mbp1 with Swi6 and DNA were decoupled from the Whi5-based SBF inhibition, thereby reducing the model to two distinct modules governed by mass-action kinetics, which we solved at steady state (Figure 6A, see STAR Methods and Supplemental Information for details):

1) an SBF/MBF binding module that computed the concentrations of DNA-bound and -free SBF/MBF complexes (as dimers of heterodimers), and the fractions of SBF- and MBF-bound G1/S promoters in the nucleus as a function of cell size;
2) a phosphorylation module that integrated the cell size-dependent output of the first module to predict the size at which the Whi5-SBF inhibitory interaction was alleviated to trigger Start.

Assigning the total concentrations of the SBF and MBF subunits to the values determined by sN&B (including the observed variability), and assuming 200 target gene promoters,

Figure 6. A Mathematical Model of Start Constrained by Quantitative sN&B Values

(A) Schematic of the simplified model for Start. In the SBF/MBF binding module, the concentrations of Mbp1, Swi6, and Whi5 are size independent. Swi4 and Mbp1 can bind target promoter DNA either free of Swi6 (solid lines) or as fully formed hetero-tetramer SBF or MBF complexes (dotted lines). Effective dissociation constants for protein-protein and protein-DNA interactions are indicated next to each line and expressed as microscopic Swi4 or Mbp1 monomer-DNA ($K_{s,m1}$), Swi4, or Mbp1 monomer-Swi6 monomer ($K_{s,m2}$) constants and putative Swi4 or Mbp1 dimer-DNA dissociation constants ($K_{s,m3}$). The output from the SBF/MBF binding module (i.e., concentrations of DNA-bound and DNA-free SBF/MBF) is used as an input in the phosphorylation module, which is solved for the Whi5-SBF dissociation constant, K_{ws}. An increase in the fraction of uninhibited SBF-bound DNA target sites increases the likelihood of *CLN1/2* transcription, and amplification of phosphorylation on Whi5 and Swi6, which increases K_{ws} and thereby releases Whi5 from SBF at G1/S promoters to trigger Start.

(B) The concentrations of SBF bound by DNA (green) and MBF bound by DNA (orange) versus cell size.

(C) The fraction of total G1/S promoter sites bound by SBF and MBF (black), MBF alone (orange) or SBF alone (green) versus cell size.

(D) Left-hand (black line) and right-hand (purple curves) sides of Equation 4 as a function of the Whi5-SBF dissociation constant K_{ws} as cells grow from small (light purple) to large (dark purple) sizes. Possible stable cellular states (solutions of Equations 4 and 5) are intersections of the size-independent black line and size-dependent sigmoids.

(E) Plot of the largest solution of Equation 4, K_{ws}^{**} as a function of cell size for small cells (light purple line, Whi5-SBF complex stable) to larger cells (dark purple line, Whi5-SBF complex unstable) at a critical size V*.

(F) Box and whisker plots of simulated critical cell size for WT and *mbp1Δ* cells in glucose (blue) versus glycerol (red) for nuclear concentrations of Swi4, Swi6, Mbp1, and Whi5 randomly picked within the ranges constrained by sN&B measurements (see Supplemental Information and STAR Methods). Equations were solved to find the critical size at Start (V*) for each parameterized cell, and 100 such values used to generate the box and whisker plots for each condition. Differences (*, **, ***) in simulated critical sizes were all statistically significant ($p < 0.001$).

we solved the SBF/MBF binding module as a function of cell size. For WT cells in glucose and for default values of the relevant affinities, including affinities of Swi4 and Mbp1 for Swi6 (see Supplemental Information and STAR Methods), the fraction of SBF bound to DNA exhibited a shallow peak at intermediate size (Figure 6B), consistent with experimental observations of the SBF-DNA interaction (Harrington and Andrews, 1996; Koch et al., 1996), and indicating that this metric alone was unlikely to be a decisive determinant of Start. In contrast, the fraction of SCB/MCB-containing promoters occupied by SBF increased significantly with cell growth, while the fraction of promoters occupied by MBF remained largely unchanged (Figure 6C). This progressive increase in promoter occupancy was due to the large increase in Swi4 copy number, along with a more modest Swi6 increase, as a function of cell growth. Thus, in large cells, promoter DNA was predominantly bound by SBF.

In the second module, Whi5-SBF dissociation was assumed to occur upon phosphorylation by Cln1/2-Cdc28 at a critical number of sites on Whi5 and Swi6 (Costanzo et al., 2004; De Bruin et al., 2004; Wagner et al., 2009), corresponding to a dissociation constant, denoted K_{ws}, which depended on phosphorylation activity in a sigmoid-like fashion (Equation 4, STAR Methods). In turn, this phosphorylation activity depended upon the probability of active SBF/MBF at the *CLN1/2* promoters, and hence on both the fractions of SBF- and MBF-bound target promoters (denoted f_{SBF} and f_{MBF}) and on Whi5-SBF dissociation, such that f_{SBF} was modulated by the fraction of active SBF complexes, $f_{Whi5-free}$ (K_{ws}). Using the simplest model in which the phosphorylation activity was proportional to these fractions (Equation 5), the phosphorylation module reduced to the system of equations for K_{ws}:

$$\frac{K_{ws}}{K_0} = \frac{p^M}{1 + p + p^2 + \ldots p^M}, \qquad \text{(Equation 4)}$$

where the phosphorylation activity p depended on cell size, protein expression levels, and also K_{ws} itself in a non-trivial way;

$$p = \frac{f_{SBF}(size) * f_{Whi5-free}(K_{ws}, size)}{\alpha} + \frac{f_{MBF}(size)}{\beta}, \qquad \text{(Equation 5)}$$

where K_0, α, and β are normalization constants. Note that the resolution of the SBF/MBF binding module provided explicit solutions for f_{SBF}, $f_{Whi5-free}$ and f_{MBF} for any given cell size, so that, once the parameters α and β are fixed, K_{ws} was the only unknown of the system of equations. Equations 4 and 5 thus defined an implicit relation between K_{ws} and cell size.

For illustrative purposes, we represented the left- and right-hand sides of Equation 4 as a function of K_{ws} for two different cell sizes (Figure 6D, respectively, black and purple curves), such that the model solution occurred where the plots intersect. At any size, there was always a solution in the region where K_{ws} was smaller than the Swi4-Swi6 and Whi5 protein concentrations, and where Whi5 remained bound to SBF, i.e., pre-Start conditions. In contrast, a solution at high K_{ws} (i.e., where the Whi5/SBF complex dissociates, corresponding to Start) only existed at larger cell size. The largest of the solutions of Equations 4 and 5 as a function of cell size defined the critical size at Start V^* as the cell volume at the transition from low to high K_{ws} (Figure 6E). Exploration of the parameter space revealed that the predicted critical size only weakly depended on the specific individual K_d values as long as certain scaling conditions were fulfilled (Figures S17A–S17D and STAR Methods).

The model accurately captured the smaller size of WT cells in glycerol compared with glucose (Figure 6F, *) and the observed nutrient-dependent large size phenotype of the *mbp1Δ* strain (Figure 6F, compare ** and ***; Figure S17E). As expected, the predicted critical size was smaller in *whi5Δ* and larger in *swi4Δ* strains for glucose and glycerol medium, in quantitative agreement with size measurements. The size dependence of the G1/S transition in these two mutant backgrounds was linear rather than switch-like, also consistent with previously reported loss of Start coherence for *whi5Δ* and *swi4Δ* strains (Bean et al., 2006). The cell-to-cell critical size variability (±1–2 fL), as assessed from sensitivity analysis, was in good agreement with the variability at the population level we observed in experimental size measurements (Figures S8A–S8C). Thus, the model predicted that the proposed mechanism for Start buffers against moderate ~20–25 nM variations in Start regulator abundance, such that the variability in critical size was on the order of only 5%–10%. Under the assumption of similar protein concentrations in haploid and diploid cells, the model also recapitulated the observed ~2-fold larger cell size for diploid cells, which contain twice as many SBF/MBF-regulated promoters and therefore require extended SBF/MBF accumulation in G1 (Figure S17E).

DISCUSSION

This analysis of the absolute concentrations and stoichiometries of the main regulators of Start by sN&B in single live budding yeast cells provides insight into the metrics that set the size threshold and how nutrients modulate these metrics.

In small cells, we find that the copy numbers of SBF and MBF complexes are severely limiting with respect to the ~200 promoters in the G1/S regulon, with an occupancy ratio of less than 30%. SBF/MBF are even more limiting in small cells with respect to the total number of SCB and MCB sites, estimated at ~400 by various criteria (Iyer et al., 2001; Wang et al., 2009; Ferrezuelo et al., 2010). In large cells, due to the size-dependent increase in copy numbers, the total amount of SBF and MBF is in excess of G1/S promoter number, and much less limiting with respect to the total number of SCB/MCB target sites. These observations suggest that titration of G1/S promoters by SBF/MBF helps to determine the timing of Start, concordant with the known increase in SCB/MCB site occupancy throughout G1 (Harrington and Andrews, 1996; Koch et al., 1996; Harris et al., 2013). Previously, it has been shown that addition of an extra ~120 SCB sites increases cell size in a manner that is counteracted by overexpression of *CLN3* (Wang et al., 2009). This result is also consistent with titration of promoter sites by SBF/MBF since, at any given level of site saturation by SBF/MBF, the probability of activation should increase with Cln3 concentration. Indeed, *swi4Δ/SWI4* heterozygous diploids have a large cell size (McInerny et al., 1997) and overexpression of hyperactive truncated allele of *SWI4* can accelerate Start (Sidorova and

Breeden, 2002). These observations, in conjunction with the present quantitative sN&B results, collectively support a model in which saturation of G1/S regulon promoters by SBF/MBF constitutes a determinant of the size at which Start occurs.

Our finding that absolute Whi5 concentration is constant with respect to both size and time throughout G1 phase is in agreement with previous reports (Costanzo et al., 2004; De Bruin et al., 2004; Ferrezuelo et al., 2012), but contradicts a recent proposal that Start is triggered by Whi5 dilution (Schmoller et al., 2015). While our results demonstrate that Whi5 continues to be synthesized throughout G1 phase, both scenarios—a constant Whi5 with increasing Swi4 versus dilution of Whi5 with constant Swi4—result in a diminishing Whi5 to Swi4 ratio throughout G1, which, as our mathematical model shows, will impact the timing of Start. Since Swi4 protein appears to be quite stable (Christiano et al., 2014), its accumulation throughout G1 phase is likely driven by previously documented G1-periodic transcription of *SWI4* (Foster et al., 1993; McInerny et al., 1997; MacKay et al., 2001). The marked amplification of Swi4 levels as cells progress through G1 phase may reflect a potential *SWI4*-positive feedback loop (Harris et al., 2013).

The increase we observe in the levels of all SBF and MBF subunits, in particular Mbp1, in glycerol medium provides new insight into how the Start transcriptional machinery is adjusted to cope with poorer carbon sources. Specifically, this upregulation has the dual effect of increasing the ratio of SBF/MBF to G1/S promoters and of decreasing the Whi5 to SBF ratio that poises cells for relief of transcriptional inhibition. Importantly, because SBF/MBF levels respond to nutrient signals, the same titration mechanism for Start is operative in glycerol medium as in glucose medium, the only difference being that the nutrient-dependent increase in SBF, and particularly MBF, accelerates the timing of site saturation with respect to growth. This enhanced role for MBF is consistent with the increase in Cln1 levels we observe in glycerol medium. Collectively, these results suggest the size threshold is set at least in part by the rate of accumulation of SBF and MBF under different conditions and explain why nutrient-dependent size control operates in the absence of the Cln3/Whi5/Bck2 axis (Costanzo et al., 2004). The mechanisms by which growth and nutrient signaling pathways modulate SBF and MBF levels, as well as the precise role of competition between SBF and MBF for different G1/S promoters, remain to be determined.

Our mathematical model of the Start transition extends previous models based solely on the relief of SBF/MBF inhibition by Cln-Cdc28-mediated phosphorylation and Whi5 nuclear export (Cross et al., 2002; Di Talia et al., 2009; Huang et al., 2009; Wang et al., 2009; Charvin et al., 2010; Adames et al., 2015; Liu et al., 2015; Laomettachit et al., 2016; Palumbo et al., 2016; Aldea et al., 2017) by incorporating SBF/MBF accumulation as cells grow in G1 phase and the enhanced expression of SBF/MBF in poor nutrients. Our model thus accommodates specialized functions of SBF and MBF (Hendler et al., 2017), unlike prior models that treat SBF and MBF activity as a single parameter (Laomettachit et al., 2016). We also find that Cln2 amplification is damped due to an increased contribution from MBF in glycerol medium. This result suggests that Start may be less switch-like in poor nutrients due to loss of positive feedback (Charvin et al., 2010). The quantitative assessment of Start regulators under other environmental and genetic conditions (Kaluarachchi Duffy et al., 2012; Moretto et al., 2013; VanderSluis et al., 2014; Talarek et al., 2017) will allow further clarification of the mechanisms that control this exemplar cell state transition.

STAR★METHODS

Detailed methods are provided in the online version of this paper and include the following:

- KEY RESOURCES TABLE
- CONTACT FOR REAGENT AND RESOURCE SHARING
- EXPERIMENTAL MODEL AND SUBJECT DETAILS
  - Strain Construction
- METHOD DETAILS
  - Determination of Cell Size and Critical Size at Start
  - Cell Culture and Sample Preparation for sN&B Experiments
  - Growth in Liquid Medium
  - Mounting of Cells on Agarose Pads
  - Sample Preparation for Microfluidics
  - High-Content Confocal Imaging of Whi5-GFP Cells
  - sN&B Imaging
- QUANTIFICATION AND STATISTICAL ANALYSIS
  - Image Analysis
  - Cell Segmentation
  - Definition of Regions of Interest (ROIs)
  - Probabilistic Background Removal (PBR) and Single Cell Data
  - Accuracy, Precision and Limits of sN&B
  - Mathematical Modeling
- DATA AND SOFTWARE AVAILABILITY

SUPPLEMENTAL INFORMATION

Supplemental Information includes 17 figures and 1 table and can be found with this article online at https://doi.org/10.1016/j.cels.2018.04.012.

ACKNOWLEDGMENTS

We thank Linda Breeden, Brandt Schneider, Brenda Andrews, and Mike Cook for discussions; an anonymous reviewer for helpful comments; and Sibyl Drissler and Linnea Olofsson for assistance with yeast strain construction and initial microscopy experiments. This work was supported by the Rensselaer Polytechnic Institute (to C.A.R.), the Canadian Institutes of Health Research (MOP-366608 to M.T.), the Ministère de l'enseignement supérieur, de la recherche, de la science et de la technologie du Québec through Génome Québec (to M.T.), the Canada Foundation for Innovation (30789 and 31072 to M.T.), and by a Canada Research Chair in Systems and Synthetic Biology (to M.T.).

AUTHOR CONTRIBUTIONS

Conceptualization, C.A.R., M.T., and S.T.; Methodology, C.A.R., M.T., S.N., and S.T.; Investigation, S.D., S.T., and L.B.; Formal Analysis, S.D., S.T., and C.A.R.; Writing – Original Draft, C.A.R., M.T., S.D., and S.T.; Writing – Review & Editing, C.A.R., S.T., and M.T.; Resources, J.C. and S.T.; Supervision, C.A.R. and M.T.; Funding Acquisition, C.A.R. and M.T.

DECLARATION OF INTERESTS

The authors declare no competing interests.

Received: December 6, 2017
Revised: March 17, 2018
Accepted: April 25, 2018
Published: May 23, 2018

REFERENCES

Adames, N.R., Schuck, P.L., Chen, K.C., Murali, T.M., Tyson, J.J., and Peccoud, J. (2015). Experimental testing of a new integrated model of the budding yeast Start transition. Mol. Biol. Cell *26*, 3966–3984.

Aldea, M., Jenkins, K., and Csikász-Nagy, A. (2017). Growth rate as a direct regulator of the start network to set cell size. Front. Cell Dev. Biol. *5*, 57.

Amigoni, L., Colombo, S., Belotti, F., Alberghina, L., and Martegani, E. (2015). The transcription factor Swi4 is target for PKA regulation of cell size at the G1 to S transition in *Saccharomyces cerevisiae*. Cell Cycle *14*, 2429–2438.

Baetz, K., and Andrews, B. (1999). Regulation of cell cycle transcription factor Swi4 through auto-inhibition of DNA binding. Mol. Cell. Biol. *19*, 6729–6741.

Baroni, M., Monti, P., and Alberghina, L. (1994). Repression of growth-regulated G1 cyclin expression by cyclic AMP in budding yeast. Nature *371*, 339–342.

Bean, J.M., Siggia, E.D., and Cross, F.R. (2005). High functional overlap between MluI cell-cycle box binding factor and Swi4/6 cell-cycle box binding factor in the G1/S transcriptional program in *Saccharomyces cerevisiae*. Genetics *171*, 49–61.

Bean, J.M., Siggia, E.D., and Cross, F.R. (2006). Coherence and timing of cell cycle Start examined at single-cell resolution. Mol. Cell *21*, 3–14.

Bourges, A.C., Torres Montaguth, O.E., Ghosh, A., Tadesse, W.M., Declerck, N., Aertsen, A., and Royer, C.A. (2017). High pressure activation of the Mrr restriction endonuclease in *Escherichia coli* involves tetramer dissociation. Nucleic Acids Res. *45*, 5323–5332.

de Bruin, R.A.M., Kalashnikova, T.I., Chahwan, C., McDonald, W.H., Wohlschlegel, J., Yates, J., Russell, P., and Wittenberg, C. (2006). Constraining G1-specific transcription to late G1 phase: the MBF-associated corepressor Nrm1 acts via negative feedback. Mol. Cell *23*, 483–496.

De Bruin, R.A., McDonald, W.H., Kalashnikova, T.I., Yates, J., and Wittenberg, C. (2004). Cln3 activates G1-specific transcription via phosphorylation of the SBF bound repressor Whi5. Cell *117*, 887–898.

Charvin, G., Oikonomou, C., Siggia, E.D., and Cross, F.R. (2010). Origin of irreversibility of cell cycle Start in budding yeast. PLoS Biol. *8*, e1000284.

Christiano, R., Nagaraj, N., Fröhlich, F., and Walther, T.C. (2014). Global proteome turnover analyses of the yeasts *S. cerevisiae* and *S. pombe*. Cell Rep. *9*, 1959–1966.

Cormack, B.P., Valdivia, R.H., and Falkow, S. (1996). FACS-optimized mutants of the green fluorescent protein (GFP). Gene *173*, 33–38.

Costanzo, M., Nishikawa, J.L., Tang, X., Millman, J.S., Schub, O., Breitkreuz, K., Dewar, D., Rupes, I., Andrews, B., and Tyers, M. (2004). CDK activity antagonizes Whi5, an inhibitor of G1/S transcription in yeast. Cell *117*, 899–913.

Cross, F.R., Archambault, V., Miller, M., and Klovstad, M. (2002). Testing a mathematical model of the yeast cell cycle. Mol. Biol. Cell *13*, 52–70.

Dechant, R., Saad, S., Ibáñez, A.J., and Peter, M. (2014). Cytosolic pH regulates cell growth through distinct gtpases, Arf1 and Gtr1, to promote ras/PKA and TORC1 activity. Mol. Cell *55*, 409–421.

Deleeuw, L., Tchernatynskaia, A.V., and Lane, A.N. (2008). Thermodynamics and specificity of the Mbp1–DNA interaction. Biochemistry *47*, 6378–6385.

Digman, M.A., Dalal, R., Horwitz, A.F., and Gratton, E. (2008). Mapping the number of molecules and brightness in the laser scanning microscope. Biophys. J. *94*, 2320–2332.

Digman, M.A., Stakic, M., and Gratton, E. (2013). Raster image correlation spectroscopy and number and brightness analysis. Methods Enzymol. *518*, 121–144.

Dungrawala, H., Hua, H., Wright, J., Abraham, L., Kasemsri, T., McDowell, A., Stilwell, J., and Schneider, B.L. (2012). Identification of new cell size control genes in *S. cerevisiae*. Cell Div. *7*, 24.

Eriksson, P.R., Ganguli, D., and Clark, D.J. (2011). Spt10 and Swi4 control the timing of histone H2A/H2B gene activation in budding yeast. Mol. Cell. Biol. *31*, 557–572.

Eser, U., Falleur-Fettig, M., Johnson, A., and Skotheim, J.M. (2011). Commitment to a cellular transition precedes genome-wide transcriptional change. Mol. Cell *43*, 515–527.

Ettinger, A., and Wittmann, T. (2015). Flourescence live cell imaging. Methods Cell Biol. *123*, 77–94.

Ferguson, M.L., Le Coq, D., Jules, M., Aymerich, S., Declerck, N., and Royer, C.A. (2011). Absolute quantification of gene expression in individual bacterial cells using two-photon fluctuation microscopy. Anal. Biochem. *419*, 250–259.

Ferguson, M.L., Le Coq, D., Jules, M., Aymerich, S., Radulescu, O., Declerck, N., and Royer, C.A. (2012). Reconciling molecular regulatory mechanisms with noise patterns of bacterial metabolic promoters in induced and repressed states. Proc. Natl. Acad. Sci. USA *109*, 155–160.

Ferrezuelo, F., Aldea, M., and Futcher, B. (2009). Bck2 is a phase-independent activator of cell cycle-regulated genes in yeast. Cell Cycle *8*, 239–252.

Ferrezuelo, F., Colomina, N., Futcher, B., and Aldea, M. (2010). The transcriptional network activated by Cln3 cyclin at the G1-to-S transition of the yeast cell cycle. Genome Biol. *11*, R67.

Ferrezuelo, F., Colomina, N., Palmisano, A., Garí, E., Gallego, C., Csikász-Nagy, A., and Aldea, M. (2012). The critical size is set at a single-cell level by growth rate to attain homeostasis and adaptation. Nat. Commun. *3*, 1012.

Flick, K., Chapman-Shimshoni, D., Stuart, D., Guaderrama, M., and Wittenberg, C. (1998). Regulation of cell size by glucose is exerted via repression of the CLN1 promoter. Mol. Cell. Biol. *18*, 2492–2501.

Foster, R., Mikesell, G.E., and Breeden, L. (1993). Multiple SWI6-dependent cis-acting elements control SWI4 transcription through the cell cycle. Mol. Cell. Biol. *13*, 3792–3801.

Ghaemmaghami, S., Huh, W., Bower, K., Howson, R.W., Belle, A., Dephoure, N., and Weissman, J.S. (2003). Global analysis of protein expression in yeast. Nature *425*, 737–741.

Ginzberg, M.B., Kafri, R., and Kirschner, M. (2015). On being the right (cell) size. Science *348*, 771.

Harrington, L.A., and Andrews, B.J. (1996). Binding to the yeast Swi4,6-dependent cell cycle box, CACGAAA, is cell cycle regulated in vivo. Nucleic Acids Res. *24*, 558–565.

Harris, M.R., Lee, D., Farmer, S., Lowndes, N.F., and de Bruin, R.A.M. (2013). Binding specificity of the G1/S transcriptional regulators in budding yeast. PLoS One *8*, 1–8.

Hartwell, L.H., Culotti, J., Pringle, J.R., and Reid, B.J. (1974). Genetic control of the cell division cycle in yeast. Science *183*, 46–51.

Hendler, A., Medina, E.M., Kishkevich, A., Abu-Qarn, M., Klier, S., Buchler, N.E., de Bruin, R.A.M., and Aharoni, A. (2017). Gene duplication and co-evolution of G1/S transcription factor specificity in fungi are essential for optimizing cell fitness. PLoS Genet. *13*, 1–24.

Huang, D., Kaluarachchi, S., Van Dyk, D., Friesen, H., Sopko, R., Ye, W., Bastajian, N., Moffat, J., Sassi, H., Costanzo, M., et al. (2009). Dual regulation by pairs of cyclin-dependent protein kinases and histone deacetylases controls G1 transcription in budding yeast. PLoS Biol. *7*, e1000188.

Huh, W.-K., Falvo, J., Gerke, L., Carroll, A., Howson, R., Weissman, J., and O'Shea, E. (2003). Global analysis of protein localization in budding yeast. Nature *425*, 686–691.

Iyer, V.R., Horak, C.E., Scafe, C.S., Botstein, D., Snyder, M., and Brown, P.O. (2001). Genomic binding sites of the yeast cell-cycle transcription factors SBF and MBF. Nature *409*, 533–538.

Johnston, G., Pringle, J., and Hartwell, L.H. (1977). Coordination of growth with cell division in the yeast. Exp. Cell Res. *105*, 79–98.

Johnston, G.C., Ehrhardt, C.W., Lorincz, A., and Carter, B.L. (1979). Regulation of cell size in the yeast *Saccharomyces cerevisiae*. J. Bacteriol. *137*, 1–5.

Jorgensen, P., and Tyers, M. (2004). How cells coordinate growth and division. Curr. Biol. *14*, R1014–R1027.

Jorgensen, P., Nishikawa, J.L., Breitkreutz, B.-J., and Tyers, M. (2002). Systematic identification of pathways that couple cell growth and division in yeast. Science *297*, 395–400.

Jorgensen, P., Rupeš, I., Sharom, J.R., Schneper, L., Broach, J.R., and Tyers, M. (2004). A dynamic transcriptional network communicates growth potential to ribosome synthesis and critical cell size. Genes Dev. *18*, 2491–2505.

Jorgensen, P., Edgington, N.P., Schneider, B.L., Rupes, I., Tyers, M., and Futcher, B. (2007). The size of the nucleus increases as yeast cells grow. Mol. Biol. Cell *18*, 3523–3532.

Kaluarachchi Duffy, S., Friesen, H., Baryshnikova, A., Lambert, J.P., Chong, Y.T., Figeys, D., and Andrews, B. (2012). Exploring the yeast acetylome using functional genomics. Cell *149*, 936–948.

Kaplan, C., and Ewers, H. (2015). Optimized sample preparation for single-molecule localization-based superresolution microscopy in yeast. Nat. Protoc. *10*, 1007–1021.

Koch, C., Moll, T., Neuberg, M., Ahorn, H., and Nasmyth, K. (1993). A role for the transcription factors Mbp1 and Swi4 in progression from G1 to S phase. Science *261*, 1551–1557.

Koch, C., Schleiffer, A., Ammerer, G., and Nasmyth, K. (1996). Switching transcription on and off during the yeast cell cycle: Cln/Cdc28 kmases activate bound transcription factor SBF (Swi4/Swi6) at Start, whereas Clb/Cdc28 kinases displace it from the promoter in G2. Genes Dev. *10*, 129–141.

Kouachi, S. (2006). Eigenvalues and eigenvectors of tridiagonal matrices. Electron. J. Linear Algebr. *15*, 115–133.

Kulak, N.A., Pichler, G., and Nagaraf, N. (2014). Minimal, encapsulated proteomic-sample processing applied to copy number estimation. Nat. Methods *11*, 319–324.

Laomettachit, T., Chen, K.C., Baumann, W.T., and Tyson, J.J. (2016). A model of yeast cell-cycle regulation based on a standard component modeling strategy for protein regulatory networks. PLoS One *11*, 1–43.

Larson, D.R., Zenklusen, D., Wu, B., Chao, J.A., and Singer, R.H. (2011). Real-time observation of transcription and elongating on an endogenous yeast gene. Science *332*, 475–478.

Leitao, R.M., and Kellogg, D.R. (2017). The duration of mitosis and daughter cell size are modulated by nutrients in budding yeast. J. Cell Biol. *216*, 3463–3470.

Lempiäinen, H., Uotila, A., Urban, J., Dohnal, I., Ammerer, G., Loewith, R., and Shore, D. (2009). Sfp1 interaction with TORC1 and Mrs6 reveals feedback regulation on TOR signaling. Mol. Cell *33*, 704–716.

Lengronne, A., and Schwob, E. (2002). The yeast CDK inhibitor Sic1 prevents genomic instability by promoting replication origin licensing in late G1. Mol. Cell *9*, 1067–1078.

Liu, X., Wang, X., Yang, X., Liu, S., Jiang, L., Qu, Y., Hu, L., Ouyang, Q., and Tang, C. (2015). Reliable cell cycle commitment in budding yeast is ensured by signal integration. eLife *4*, e03977.

Lorincz, A., and Carter, B.L.A. (1979). Control of cell size at bud initiation in *Saccharomyces cerevisiae*. J. Gen. Microbiol. *113*, 287–295.

Lucena, R., Alcaide-Gavilan, M., Schubert, K., He, M., Domnauer, M.G., Marquer, C., Close, C., Surma, M.A., and Kellogg, D.R. (2018). Cell size and growth rate are modulated by TORC2-dependent signals. J. Cell. Biol. *28*, 196–210.

MacKay, V.L., Mai, B., Waters, L., and Breeden, L.L. (2001). Early cell cycle box-mediated transcription of CLN3 and SWI4 contributes to the proper timing of the G1-to-S transition in budding yeast. Mol. Cell. Biol. *21*, 4140–4148.

Magde, D., Elson, E., and Webb, W.W. (1974). Fluorescence correlation spectroscopy. 2. Experimental realization. Biopolymers *13*, 29–61.

McInerny, C.J., Partridge, J.F., Mikesell, G.E., Creemer, D.P., and Breeden, L.L. (1997). A novel Mcm1-dependent element in the SWI4, CLN3, CDC6, and CDC47 promoters activates M/G1-specific transcription. Genes Dev. *11*, 1277–1288.

Megerle, J.A., Fritz, G., Gerland, U., Jung, K., and Rädler, J.O. (2008). Timing and dynamics of single cell gene expression in the arabinose utilization system. Biophys. J. *95*, 2103–2115.

Miles, S., Croxford, M.W., Abeysinghe, A.P., and Breeden, L.L. (2016). Msa1 and Msa2 modulate G1-specific transcription to promote G1 arrest and the transition to quiescence in budding yeast. PLoS Genet. *12*, 1–27.

Moretto, F., Sagot, I., Daignan-Fornier, B., and Pinson, B. (2013). A pharmaco-epistasis strategy reveals a new cell size controlling pathway in yeast. Mol. Syst. Biol. *9*, 707.

Nash, R., Tokiwa, G., Anand, S., Erickson, K., and Futcher, A.B. (1988). The WHI1+ gene of *Saccharomyces cerevisiae* tethers cell division to cell size and is a cyclin homolog. EMBO J. *7*, 4335–4346.

Nasmyth, K., and Dirick, L. (1991). The role of SWI4 and SWI6 in the activity of G1 cyclins in yeast. Cell *66*, 995–1013.

Palumbo, P., Vanoni, M., Cusimano, V., Busti, S., Marano, F., Manes, C., and Alberghina, L. (2016). Whi5 phosphorylation embedded in the G1/S network dynamically controls critical cell size and cell fate. Nat. Commun. *7*, 11372.

Partridge, J.F., Mikesell, G.E., and Breeden, L.L. (1997). Cell cycle-dependent transcription of CLN1 involves Swi4 binding to MCB- like elements. J. Biol. Chem. *272*, 9071–9077.

Richardson, H.E., Wittenberg, C., Cross, F., and Reed, S.I. (1989). An essential G1 function for cyclin-like proteins in yeast. Cell *59*, 1127–1133.

Schmoller, K.M., Turner, J.J., Kõivomägi, M., and Skotheim, J.M. (2015). Dilution of the cell cycle inhibitor Whi5 controls budding-yeast cell size. Nature *526*, 268–272.

Schneider, B.L., Patton, E.E., Lanker, S., Mendenhall, M.D., Wittenberg, C., Futcher, B., and Tyers, M. (1998). Yeast G1 cyclins are unstable in G1 phase. Nature *395*, 86–89.

Schneider, B.L., Zhang, J., Markwardt, J., Tokiwa, G., Volpe, T., Honey, S., and Futcher, B. (2004). Growth rate and cell size modulate the synthesis of, and requirement for, G1-phase cyclins at start. Mol. Cell. Biol. *24*, 10802–10813.

Shaner, N.C. (2014). Fluorescent proteins for quantitative microscopy. Important properties and practical evaluation. Methods Cell Biol. *123*, 95–111.

Sidorova, J.M., and Breeden, L.L. (2002). Precocious S-phase entry in budding yeast prolongs replicative state and increases dependence upon Rad53 for viability. Genetics *160*, 123–136.

Siegmund, R.F., and Nasmyth, K.A. (1996). The *Saccharomyces cerevisiae* Start-specific transcription factor Swi4 interacts through the ankyrin repeats with the mitotic Clb2/Cdc28 kinase and through its conserved carboxy terminus with Swi6. Mol. Cell. Biol. *16*, 2647–2655.

Silljé, H.H.W., Ter Schure, E.G., Rommens, A.J.M., Huls, P.G., Woldringh, C.L., Verkleij, A.J., Boonstra, J., and Verrips, C.T. (1997). Effects of different carbon fluxes on G1 phase duration, cyclin expression, and reserve carbohydrate metabolism in *Saccharomyces cerevisiae*. J. Bacteriol. *179*, 6560–6565.

Simon, I., Barnett, J., Hannett, N., Harbison, C.T., Rinaldi, N.J., Volkert, T.L., Wyrick, J.J., Zeitlinger, J., Gifford, D.K., Jaakkola, T.S., et al. (2001). Serial regulation of transcriptional regulators in the yeast cell cycle. Cell *106*, 697–708.

Singh, J., and Tyers, M. (2009). A Rab escort protein integrates the secretion system with TOR signaling and ribosome biogenesis. Genes Dev. *23*, 1944–1958.

Skotheim, J.M., Di Talia, S., Siggia, E.D., and Cross, F.R. (2008). Positive feedback of G1 cyclins ensures coherent cell cycle entry. Nature *454*, 291–296.

Smith, W.R., and Missen, R.W. (1982). Chemical Equilibrium Analysis (John Wiley and Sons).

Soifer, I., and Barkai, N. (2014). Systematic identification of cell size regulators in budding yeast. Mol. Syst. Biol. *10*, 761.

Talarek, N., Gueydon, E., and Schwob, E. (2017). Homeostatic control of start through negative feedback between Cln3-Cdk1 and Rim15/greatwall kinase in budding yeast. Elife *6*, 1–21.

Di Talia, S., Wang, H., Skotheim, J.M., Rosebrock, A.P., Futcher, B., and Cross, F.R. (2009). Daughter-specific transcription factors regulate cell size control in budding yeast. PLoS Biol. *7*, e1000221.

Taylor, I.A., McIntosh, P.B., Pala, P., Treiber, M.K., Howell, S., Lane, A.N., and Smerdon, S.J. (2000). Characterization of the DNA-binding domains from the

yeast cell-cycle transcription factors Mbp1 and Swi4. Biochemistry *39*, 3943–3954.

Tokiwa, G., Tyers, M., Volpe, T., and Futcher, B. (1994). Inhibition of G1 cyclin activity by the Ras/cAMP pathway in yeast. Nature *371*, 342–345.

Travesa, A., Kalashnikova, T.I., de Bruin, R.A., Cass, S.R., Chahwan, C., Lee, D.E., Lowndes, N.F., and Wittenberg, C. (2013). Repression of G1/S transcription is mediated via interaction of the GTB motifs of Nrm1 and Whi5 with Swi6. Mol. Cell. Biol. *33*, 1476–1486.

Turner, J.J., Ewald, J.C., and Skotheim, J.M. (2012). Cell size control in yeast. Curr. Biol. *22*, R350–R359.

Tyers, M., Tokiwa, G., Nash, R., and Futcher, B. (1992). The Cln3-Cdc28 kinase complex of *S. cerevisiae* is regulated by proteolysis and phosphorylation. EMBO J. *11*, 1773–1784.

Tyers, M., Tokiwa, G., and Futcher, B. (1993). Comparison of the *Saccharomyces cerevisiae* G1 cyclins: Cln3 may be an upstream activator of Cln1, Cln2 and other cyclins. EMBO J. *12*, 1955–1968.

VanderSluis, B., Hess, D.C., Pesyna, C., Krumholz, E.W., Syed, T., Szappanos, B., Nislow, C., Papp, B., Troyanskaya, O.G., Myers, C.L., et al. (2014). Broad metabolic sensitivity profiling of a prototrophic yeast deletion collection. Genome Biol. *15*, 1–18.

Wagner, M.V., Smolka, M.B., de Bruin, R.A.M., Zhou, H., Wittenberg, C., and Dowdy, S.F. (2009). Whi5 regulation by site specific CDK-phosphorylation in *Saccharomyces cerevisiae*. PLoS One *4*, e4300.

Wang, H., Carey, L.B., Ying, C., Wijnen, H., and Futcher, B. (2009). Recruitment of Cln3 cyclin to promoters controls cell cycle entry via histone deacetylase and other targets. PLoS Biol. *7*, e1000189.

Wood, E., and Nurse, P. (2015). Sizing up to divide: mitotic cell-size control in fission yeast. Annu. Rev. Cell Dev. Biol. *31*, 11–29.

Yahya, G., Parisi, E., Flores, A., Gallego, C., and Aldea, M.M.M. (2014). A Whi7-anchored loop controls the G1 Cdk-cyclin complex at start. Mol. Cell *53*, 115–126.

Zhang, J., Schneider, C., Ottmers, L., Rodriguez, R., Day, A., Markwardt, J., and Schneider, B.L. (2002). Genomic scale mutant hunt identifies cell size homeostasis genes in *S. cerevisiae*. Curr. Biol. *12*, 1992–2001.

STAR★METHODS

KEY RESOURCES TABLE

REAGENT or RESOURCE	SOURCE	IDENTIFIER
Chemicals, Peptides, and Recombinant Proteins		
Fluorescein Alexa647-succinimidyl ester	Spectrum Chemical Invitrogen	CAS 2321-07-5 A20006
Experimental Models: Organisms/Strains		
BY4741 *MAT***a** *his3Δ1 leu2Δ0 met15Δ0 ura3Δ0*	S288C-derived strain, parental strain for the Euroscarf *MAT***a** haploid gene deletion collection	BY4741
BY4742 *MATα his3Δ1 leu2Δ0 lys2Δ0 ura3Δ0*	S288C-derived strain, parental strain for the Euroscarf *MATα* haploid gene deletion collection	BY4742
mbp1Δ *mpb1ΔkanMX*	Euroscarf haploid gene deletion collection	Y03753
swi4Δ *swi4ΔkanMX*	Euroscarf haploid gene deletion collection	Y06109
SWI4-GFP *swi4::SWI4-mGFPmut3-HIS3MX*	This study	MTY5000
MBP1-GFP *mbp1::MBP1-mGFPmut3-HIS3MX*	This study	MTY5003
SWI6-GFP *swi6::SWI6-mGFPmut3-HIS3MX*	This study	MTY5006
WHI5-GFP *whi5::WHI5-mGFPmut3-HIS3MX*	This study	MTY5009
GFP alone *BY4741 - pGAL-mGFPmut3-CEN-URA3*	This study	MTY5012
CLN1-GFP *cln1::CLN1-mGFPmut3-HIS3MX*	This study	MTY5013
CLN1-GFP swi4Δ *cln1::CLN1-mGFPmut3-HIS3MX swi4ΔkanMX*	This study	MTY5014
CLN1-GFP mbp1Δ *cln1::CLN1-mGFPmut3-HIS3MX mpb1ΔkanMX*	This study	MTY5018
CLN2-GFP *cln2::CLN2-mGFPmut3-HIS3MX*	This study	MTY5021
CLN2-GFP swi4Δ *cln2::CLN2-mGFPmut3-HIS3MX swi4ΔkanMX*	This study	MTY5022
CLN2-GFP mbp1Δ *cln2::CLN2-mGFPmut3-HIS3MX mpb1ΔkanMX*	This study	MTY5025
WHI5-GFP(S65T) *whi5::WHI5-GFP(S65T)-natMX*	J. Nishikawa, PhD thesis	MTY4025
WHI5-GFP(S65T) mbp1Δ *whi5::WHI5-GFP(S65T)-natMX mpb1ΔkanMX*	This study	MTY5028
WT diploid BY4741 x BY4742	This study	MTY5029
WHI5-GFP(S65T) *MAT***a** *whi5::WHI5-GFP(S65T)- kanMX* (W303**a** background)	Costanzo et al., 2004	MTY3001
Software and Algorithms		
sN&B analysis routines - MATLAB	This study	N/A
Mathematical modeling routines - MATLAB	This study	N/A

CONTACT FOR REAGENT AND RESOURCE SHARING

Further information and requests for resources and reagents should be directed to and will be fulfilled by the Lead Contact, Catherine Royer (royerc@rpi.edu) for imaging and analysis and Mike Tyers (md.tyers@umontreal.edu) for yeast strains and modeling.

EXPERIMENTAL MODEL AND SUBJECT DETAILS

Strain Construction

All strains were generated in the S288C BY4741 background by integration of an *mGFPmut3-HIS3MX* cassette (referred to as GFP throughout the text for simplicity) at the C terminus of the *SWI4*, *SWI6*, *MBP1*, *WHI5*, *CLN1* and *CLN2* loci, which were crossed into other mutant strain backgrounds as needed (Key Resources Table). The free GFP strain was obtained by transformation of a <*pGAL1-mGFPmut3 CEN URA3*> plasmid into BY4741. None of the strains used in this study exhibited any noticeable phenotypic difference with the untagged BY4741 parental strain as assessed by growth rate, cell size or DNA content distribution, indicating that fusion proteins were able to complement relevant phenotypes for this study (Figure S8A). A WT diploid strain was constructed by mating to BY4742 (Key Resources Table).

METHOD DETAILS

Determination of Cell Size and Critical Size at Start

Strains were sized in early log-phase at a cell density 0.8-3.0 x 10^6 cells/mL in glycerol medium and 3.0-8.0 x 10^6 cells/mL in glucose medium using a Coulter Z2 Multisizer (Beckman-Coulter). To estimate the critical cell size, we calculated the fraction of pre-Start cells with nuclear Whi5 in each total log-phase population of thousands of WT, *mbp1Δ* or *swi4Δ* cells expressing Whi5-GFP(S65T) grown on either SC+2% glucose or SC+3% glycerol and imaged on an Opera high-content confocal screening platform (PerkinElmer). In parallel, we converted the size distributions of WT, *mbp1Δ and swi4Δ* strains to cumulative distributions to reveal the cut-off size corresponding to this critical fraction, which we identified as the critical size at Start (Figure S8).

Cell Culture and Sample Preparation for sN&B Experiments

Synthetic complete (SC) dropout medium (SC: 6.7 g/L yeast nitrogen base without amino acids (Sigma-Aldrich), 2 g/L amino acid mix (Sunrise Science)) was supplemented with 2% w/v glucose or 2% w/v glycerol (2-photon sN&B experiments) or 3% w/v glycerol (for 1-photon sN&B experiments and size distribution determination). For each sN&B experiment, single colonies of the untagged BY4741 parental strain, a free GFP strain and the GFP-tagged strain of interest were grown to exponential phase in selective SC dropout media supplemented with 2% glucose or 2% glycerol at 30°C. Cells were mounted onto 2% agarose pads as previously described, or loaded into a microfluidic culture chamber (CellASIC ONIX) for time-lapse experiments (see below). Cells grew more slowly in the microfluidics device than in free cultures. For the time-dependent comparison of free GFP and Whi5-GFP intensity, following growth of the *pGAL1-GFP* cells to log phase in SC+2% raffinose and 40 min GFPmut3 induction in SC+0.1% galactose, cells were washed in SC+2% glucose to halt GFP production, then grown in the same medium until OD_{600}=0.5 to prevent maturation of new GFP molecules during the beginning of imaging. Then cells were transferred into a microfluidics plate and imaged using sN&B (50 rapid raster scans with 40 μs pixel dwell time) every 20 min for 2 h under a continuous SC+2% glucose nutrient flux. Cells expressing Whi5-GFP were grown in SC+2% glucose and continually replenished with the same medium in the microfluidics device.

Growth in Liquid Medium

Single colonies of strains bearing integrated GFP fusion proteins were grown to saturation in SC-his or SC-ura medium to select for the integrated cassette or plasmid with either glucose or glycerol as a carbon source. For the final growth phase prior to each experiment cells were transferred to non-selective SC complete glucose or glycerol medium. Sample and control cultures were diluted (OD_{600} = 0.1-0.2) and grown (~5 h for glucose cultures, ~24 h for glycerol cultures) to early exponential phase (OD_{600} = 0.5). Sample and control cultures were treated identically to allow accurate correction for auto-fluorescence. For GFP induction, after initial growth to saturation the *GAL1-GFP* and control strains were washed twice in fresh medium, diluted (OD_{600} = 0.2-0.3) and grown in 2% raffinose medium for 3-4 h followed by addition of galactose (0.1%) for 1 h. Cells were then washed twice in fresh medium, diluted, and grown in glucose medium for ~5 h to exponential phase to approximate similar GFP levels, auto-fluorescence, and culture conditions for fusion protein strains. Culture size distributions were determined on Z2 Multisizer (Beckman-Coulter) after growth to log phase in non-selective SC media.

Mounting of Cells on Agarose Pads

For imaging of asynchronous cultures, cells were mounted on agarose pads essentially as previously described (Ferguson et al., 2011). A suspension of 2% agarose (UltraPure LMP agarose, Invitrogen) was melted in appropriate medium and 60 μL of the solution dispensed onto a 25mm coverslip. After ~20 min drying time, a silicone double-adhesive ring (Invitrogen) was placed onto the coverslip. Cells were gently centrifuged (1300 rpm, 1 min, 20°C), re-suspended in medium (OD_{600} = ~5) and 3 μL absorbed onto the agarose pad for ~1 min. Coated coverslips were prepared by spreading 20 μL of filter sterilized Con-A (Sigma, 2 mg/mL) on a coverslip (No. 1, VWR), drying for at least 2 h, and rinsing with sterile water (Kaplan and Ewers, 2015). To mount cells, a ConA coated

coverslip was gently pressed on top of the agarose to seal the pad against the adhesive silicon ring. Sealed pads were clamped in an AttoFluor chamber (Molecular Probes) and immediately imaged for no more than 1.5 h. This procedure allowed imaging of a monolayer of cells with small clusters of 5-20 cells under conditions of constant nutrient availability throughout the experiment.

Sample Preparation for Microfluidics

For sN&B time courses in a microfluidic chamber, Whi5-GFP, free GFP and two parental BY4741 strains for auto-fluorescence subtraction were imaged using a CellASIC ONIX Microfluidic Platform. Free GFP expression was induced by galactose as above, and cells were switched to glucose medium and allowed to grow to OD_{600} 0.5 prior to imaging to ensure that no GFP was produced during the time-course. The same pre-growth protocols were used as for sN&B on agarose pads. Cells were transferred directly from liquid log-phase cultures to the cell loading wells in a haploid microfluidics plate (CellASIC, Y04C). Culture medium (100 μL) was dispensed into all 6 medium wells to ensure homogeneous, vortex-free medium flow throughout each cell culture chamber. Cells were loaded for 30 s at 3 psi and single cells that became immobilized in the 3.5 μm chamber were allowed to grow under constant flow conditions (0.3 psi/well) while being imaged on an ISS Alba 2 photon microscope. Several fields of view (FOV) for the Whi5-GFP, free GFP and parental strains were imaged every 20 min. Whi5-GFP photo-bleaching was normalized against free GFP photo-bleaching after subtraction of background auto-fluorescence signal. Since cells grew slowly in the microfluidic device, the free GFP dilution factor over the time-course was small (~1.2-fold) compared to the total decrease in intensity (~5-fold) (Figure 3A). Based on these values, we calculated a 3.7-fold decrease in intensity due to photo-bleaching over the entire time-course.

High-Content Confocal Imaging of Whi5-GFP Cells

To determine the fraction of pre-Start cells in particular populations and to establish that there was no correlation between Whi5 concentration and cell size in the absence of a photo-bleaching effect (Figures 3G–3J), we imaged WT and *mbp1Δ* strains in the BY4741 background and WT strains in the W303 background that expressed GFP-tagged Whi5 using a high-content Opera confocal imaging platform (PerkinElmer), equipped with a Nipkow spinning-disk, using a single laser exposure at maximal power. BY4741 and W303 cells expressing Whi5-GFP(S65T) were grown to saturation from individual colonies in liquid SC medium supplemented with either 2% glucose, 3% glycerol + 3% ethanol, or 2% glycerol + 1% ethanol, in a rotary incubator in glass tubes at 30C. Then cells were diluted (1/200) in fresh medium, and cultured in a rotary incubator in glass tubes at 30°C until reaching early-to-mid log phase (0.8-3.0 x 10^6 cells/mL in glycerol medium and 3.0-8.0 x 10^6 cells/mL in glucose medium). Then 200 uL of cell solutions were directly pipetted onto a 96-well Greiner Screenstar imaging plate (triplicate, 3 wells per condition) and imaged on the Opera confocal instrument. GFP excitation was performed using a single 480-600 ms laser exposure at 488nm and maximal power, and GFP emission from tens of field of views (thousands of cells) was recorded through a 60x water immersion objective. Raw images were analyzed using custom MATLAB scripts, in which the yeast auto-fluorescence detected in the GFP channel was used to mask individual cells, while the much brighter Whi5-GFP nuclear signal was used to discriminate G1 cells and compute the cell nucleus-averaged fluorescence intensity (Figures S8D–S8G). Masking accuracy was visually controlled on a few fields of view in each condition. This masking of individual cells allowed determination of the correlation of cell size (area, in pixels) with Whi5 level (fluorescence intensity), as shown on Figure 3.

sN&B Imaging

Most sN&B acquisitions were performed on an ISS Alba fast scanning mirror fluctuation microscope (ISS, Champaign, IL) equipped with 2-photon laser excitation (Mai Tai Ti: Sapphire, Newport-SpectraPhysics, Mountain View, CA) for which the excitation wavelength was 1000 nm. Other sN&B experiments were performed on a second ISS Alba microscope equipped with a 1-photon WhiteLase supercontinuum laser (Fianium/NKT Photonics, Birkerød Denmark) for which the excitation wavelength was 488 nm. The quality of the microscope and laser alignment was ascertained for each experiment using a solution of 40 nM fluorescein in Tris buffer (pH 8.0) and which was compared to the same measurement of the fluorescein in glycerol solution performed periodically. Acquisitions were 50 raster scans per FOV with a 40 μs pixel dwell-time and FOV size of 256x256 pixels covering 20x20 μm or 64 μs dwell-time and 30x30 μm FOV size for 1-photon experiments. As a consequence, consecutive intensity measurements were made at each individual pixel only every 2.5-3 s for 2-photon experiments and 5-6s for 1-photon experiments. Each FOV was imaged in sN&B mode at 3 z-positions separated by 500 nm for 2-photon experiments or 700 nm for 1-photon experiments.

QUANTIFICATION AND STATISTICAL ANALYSIS

Given Equations 1, 2, and 3 in the main text, to calculate the concentration of a GFP-tagged protein within a given cell compartment, is it sufficient to know the pixel- and time-averaged fluorescence intensity of the GFP-tagged protein in the compartment, the monomeric GFP brightness, e_{GFP}, and the effective volume, V_{eff}. The molecular brightness of monomeric GFP was calculated daily from the intensity fluctuations in individual cells that produce free GFP using Equation 1 in the main text. Then, the final value of e_{GFP} was calculated as the mean of the monomeric free GFP molecular brightness values from 30-40 cells, grown and imaged in the same conditions as the actual samples, encompassing hundreds of thousands of pixels. This internally calibrated $e_{GFP\ value}$ incorporates any optical heterogeneities present in the BY4741 yeast cytoplasm under our experimental conditions. The standard error on the mean value of e_{GFP} on any given day was determined to be $\leq$ 2% (Figures S2). The V_{eff} was calibrated using a solution of known concentration C_F =40 nM fluorescein (determined by spectrophotometric measurements at 490 nm assuming ε =

80,000 cm^{-1} M^{-1} for fluorescein), by sN&B in a 40% glycerol solution to slow diffusion sufficiently to control for diffusional averaging during the pixel dwell-time. Application of Equation S1 (see below) to this fluorescein sN&B data yielded the number n_F of fluorescein molecules, in V_{eff}. Since the concentration, C_F, is known, the effective excitation volume, V_{eff}, can be calculated from n_F as follows:

$$n_F = (\langle F\rangle/((\sigma^2/\langle F\rangle - 1))); \; V_{eff} = n_F/(C_F \times N_A) \quad \text{(Equation S1)}$$

where N_A is Avogadro's number. Values of V_{eff} varied slightly from day-to-day due to laser alignment but were between 0.7-0.9 fL using the 2-photon excitation wavelength of 1000 nm and between 0.25-0.4 fL using the 1-photon excitation at 488 nm and a 42μm pinhole. Because we observed day to day variations in V_{eff}, as in e_{GFP}, due to microscope alignment and other variables these quantities were calibrated on each day of experiment by FCS using a 40 nM fluorescein solution in buffer as above and multiplying the value of V_{eff} determined in glycerol solution by the ratio of the G_o (time 0 FCS correlation) values obtained in buffer each day over that obtained in buffer the day the sN&B measurement was made on the glycerol solution. Any deviation of the G_o values greater than 10% prompted realignment of the microscope and a new measurement of V_{eff} by sN&B on the glycerol solution. The high level of reproducibility of the measurements from day-to-day (Figures S6 and S7) demonstrated the validity of this calibration method.

We note that unlike epi-fluorescence measurements which include substantial out of plane light, both 2-photon excitation and 1-photon confocal (the latter using a 42μm pinhole) microscopy are well-resolved in the z plane (~1-1.5 μm Gaussian extension of V_{eff} in the z-direction). As a result, the entire effective volume is enclosed even within small cellular compartments such as a yeast nucleus, provided that the compartment is in focus. Hence, uncertainty on the values of $\langle F\rangle_{FP}$ in the nucleus are mostly due to the precision of the z-focus (which is minimized by the pad mounting protocol that ensures monolayers of cells) and to a lesser extent, to photo-bleaching (see below, and Figures S1–S3).

Measurements of the absolute concentrations of the GFP fusions of the Start regulators Swi4, Whi5, Mbp1, Swi6, Cln1 and Cln2 (sometimes abbreviated as PF for protein fusions) in live yeast cells were not based on measurements of intensity fluctuations of those samples. Rather, the concentrations were calculated from the average intensity over 50 scans for all pixels in a cellular compartment (cytoplasm or nucleus) of each individual cell, $\langle F\rangle_{PF,nuc}$, the monomeric GFP brightness calibrated *in cellulo*, e_{GFP}, and the effective volume V_{eff} (see schematic in Figures 1D and S1). Then from the fluorescence fluctuations of the PF samples we determined the molecular brightness of the GFP fusions, e_{PF}, using Equation 1 in the main text. This value along with the brightness of monomeric GFP, e_{GFP}, was used to compute protein stoichiometries (Figures 2D, S11D, and S16B).

$$S = e_{PF}/e_{GFP} \quad \text{(Equation S2)}$$

The sN&B approach has been used previously for the accurate and precise measurement of fluorescent protein concentration in solution and in live bacterial cells (Ferguson et al., 2011, 2012).

Image Analysis

Despite its advantages, the low photon counts as well as detector shot noise and dark counts pose some challenges to sN&B. First, all values of N and B must be shot noise corrected. Typical shot noise corrected brightness values (see below) are fairly low, in the range of 0.0015-0.005 (auto-fluorescent background) to 0.03-0.05 (GFP) counts per dwell-time per molecule under our excitation conditions, while the uncertainty in photon counts (+/-1 over 50 frames) confers an uncertainty of 0.02 on pixel-based measured intensity and variance. Those pixel-to-pixel fluctuations were averaged out using larger regions of interest (ROI, for example all pixels inside a nucleus) to obtain reliable values of *e*. Background auto-fluorescence must also be subtracted for accurate measurements. Because we observed intra- and inter- cellular variability in the fluorescence signal detected in untagged samples (i.e., auto-fluorescence variability), we implemented a noise-removal algorithm that operates at the pixel level rather than at the level of an entire FOV. In the case of nuclear Swi4-, Swi6-, Mbp1- and Whi5-GFP, the GFP intensity was high enough such that the background contributed generally less than 10% of the intensity value. Hence, subtraction was straightforward. However, at 5-50 fold lower GFP concentrations (e.g., for Cln1/2 or the other protein fusions in the cytosol), auto-fluorescence was a prominent part of the detected signal. Thus, we applied the probabilistic background subtraction algorithm discussed below to all ROIs. Using this approach our detection limit was estimated at 1 nM GFP with 2-photon excitation and 5 nM in 1-photon excitation.

Cell Segmentation

Each .tiff image stack (50 frames over time) produced by the ISS acquisition software for each FOV was processed by the following semi-automated algorithm. First, the file stack was loaded into MATLAB using the tiffread27 script (Francois Nedelec, EMBL) and the stack projected to include all photons detected during the acquisition time-course. The resulting total intensity image was then used for segmentation of individual cells. The algorithm requires user defined inputs for 2 intensity thresholds. A hard threshold allows individual cell segregation from cell clusters but with the detriment of cropping cell borders. The algorithm performs morphological operations (dilatation/erosion, hole-filling, isolated pixel removal) and inflates each detected cell until the intensity at the border reaches the soft threshold. The software then prompts the user for approval or to input new values for the thresholds. Increasing the hard threshold allows separation of bright cell aggregates with potential loss of some dim cells, while increasing the soft threshold usually crops the cell contours, although cell masking was not very sensitive to the choice of those thresholds in general. Note that background control cells and GFP-tagged cells must be masked using approximately the same thresholds, to minimize the effect

of border pixels on average intensity/brightness. The user is allowed to manually remove cells that were badly masked, such as buds when separated from mothers, cropped mothers, cells at the border of the image, and unseparated aggregates. Once cells are segmented, the software computes the average intensity, F, variance σ^2, and shot noise-corrected brightness e and number n maps at the pixel level, using for each pixel i the photon counts $(K_i)_j$ acquired over the N=50 frames:

$$F_i = \frac{1}{N}\sum_{j=1}^{N}(K_i)_j \quad ; \quad \sigma_i^2 = \frac{1}{N-1}\sum_{j=1}^{N}\left[(K_i)_j\right]^2 - \frac{N}{N-1}(F_i)^2 \quad ; \quad e_i = \frac{\sigma_i^2}{F_i} - 1 \quad ; \quad n_i = \frac{F_i}{e_i} \qquad \text{(Equation S3)}$$

Definition of Regions of Interest (ROIs)

On occasion a few background control cells displayed a localized pattern for auto-fluorescence such as bright spots at the cell periphery or large bright blobs within the cell volume. These regions of intense auto-fluorescence were also visible in tagged-strains, though partially masked by the GFP signal, and were mostly outside the nucleus. To prevent the probabilistic background-removal algorithm from artificially reducing fluorescence intensity in the nucleus by mixing up strong nuclear signal with enhanced localized auto-fluorescence, the algorithm provides the option to manually select regions of interest, including: the nucleus (when possible, as defined by Swi4, Whi5, Mbp1 or Swi6 localization patterns), the cytosol (entire cell minus nucleus minus a sharp ring around the nucleus where the nuclear signal blurs slightly), and background blobs/spots, both in untagged and tagged strains. In a similar fashion, as we have previously done in our sN&B studies on GFP promoter fusions in bacteria (Ferguson et al., 2011, 2012), we accounted for the diameter of the excitation volume at the edges of the cell and the nucleus. To do so, in the case of the nucleus, we used a mask that was slightly smaller than the diameter of the nucleus, such that no border pixels (for which the excitation volume would not be entirely contained within the nucleus) were included in the calculations of the nuclear concentration. Then, because we did not want to include any of these border pixels in the calculation of cytoplasmic concentrations, we carried out for each cell a second calculation using a nuclear mask that was slightly larger than the nucleus. We ascertained that the effect on the calculated nuclear concentrations using a mask that was smaller than the nuclear diameter by the diameter of the excitation volume did not significantly alter the calculations because the internal nuclear concentration was quite high. However, we did note that if we used the small nuclear mask only, then pixels at the cytoplasmic nuclear border were included in the calculations of the cytoplasmic concentration and led to over-estimation of the cytoplasmic concentration (which was always much lower than the nuclear concentration). Hence, in all analyses we employed the double masking approach, first calculating the nuclear concentration with a small nuclear mask, and then calculating the cytoplasmic concentration with a large nuclear mask. As controls, a few samples were deliberately analyzed using either sharp or wide borders for the definition of the nucleus, but this did not cause significant variation in output concentrations/brightness of the nucleus. We concluded from these analyses that our results were robust to small variations in the accuracy of manual masking of the nucleus.

Probabilistic Background Removal (PBR) and Single Cell Data

Rather than an average auto-fluorescence level, the PBR algorithm aims to suppress exactly, over a set of several FOVs of tagged strains, the full distribution of pixel auto-fluorescence that is measured on a set of several FOVs from untagged strains at the individual pixel level. In practice, the algorithm computes the distribution $P_{bg}(\{F_i\})$ of stack-projected total intensities at individual pixels F_i, accumulating pixel (i) data from inside all detected cells in all untagged strain FOVs from the experiment (at least 20-30 cells, 30000-60000 pixels), and does the same for tagged-strain FOVs separately (P_{FOV}). The distributions $P_{bg}(\{F_i\})$ and $P_{FOV}(\{F_i\})$ express the probability that a pixel i within a cell shows the intensity F_i respectively in the presence of auto-fluorescence only, or auto-fluorescence and GFP. These data include as many cells as possible (from the same day of experiment, for constant imaging conditions) to cover the largest possible range of auto-fluorescence and GFP + auto-fluorescence FOV intensities and improve the accuracy of distributions. The user can manually optimize the number of bins, and visually check distributions. Owing to the statistical independence of GFP and auto-fluorescence emission, the distribution of pixel intensities in the tagged FOVs is the convolution, $P_{FOV} = P_{GFP} \otimes P_{BG}$, where P_{GFP} is the (unknown) distribution of pixel intensity due to GFP only. The algorithm computes P_{GFP} by inverting this convolution, using an iterative Newton-like numerical scheme that minimizes the least-square error between the convolution product of the measured BG distribution and the computed GFP distribution on one hand, and the measured FOV distribution on the other hand. Then, going back to individual pixels within individual cells, the algorithm computes the conditional probability that the intensity due to GFP only at pixel i is α knowing that we measured β for this pixel:

$$Pr\left(F_i^{GFP} = \alpha | F_i^{FOV} = \beta\right) = \frac{Pr\left(F_i^{GFP} = \alpha \cap F_i^{FOV} = \beta\right)}{Pr\left(F_i^{FOV} = \beta\right)} = \frac{Pr\left(F_i^{GFP} = \alpha \cap F_i^{BG} = \beta - \alpha\right)}{Pr\left(F_i^{FOV} = \beta\right)} = \frac{P_{GFP}(\alpha) * P_{bg}(\beta - \alpha)}{\sum_{\gamma=0}^{\gamma=\beta}\left[P_{GFP}(\gamma) * P_{bg}(\beta - \gamma)\right]}. \qquad \text{(Equation S4)}$$

Finally, the algorithm inverts the corresponding cumulative distribution using a Monte Carlo algorithm that generates for each pixel a random number r between 0 and 1 and finds the GFP-only contribution α such that $Pr(F_i^{GFP} \leq \alpha | F_i^{FOV} = \beta) = r$. In summary, the background-corrected image $F_i^{GFP} = \alpha$ is obtained by removing at each FOV pixel i a random contribution of the background that ensures that, overall, the pixel distribution of removed auto-fluorescence overlaps nearly perfectly with the distribution of measured auto-fluorescence (see Figure S9D). The background-corrected brightness map e_i^{GFP} could not be estimated on a pixel basis; however we performed a global (average) computation of the background brightness at the ROI level (e^{bg}) using all pixels from a given

ROI in all background images. Then, we used the fact that the two sources of variance, i.e., GFP and BG, are statistically uncorrelated to infer e_i^{GFP} from the additivity of variances:

$$\left(\sigma_i^2\right)^{FOV} = \left(\sigma_i^2\right)^{bg} + \left(\sigma_i^2\right)^{GFP} \rightarrow e_i^{GFP} = \frac{\left[e_i^{FOV} - e^{BG} * \left(1 - F_i^{GFP}/F_i^{FOV}\right)\right]}{F_i^{GFP}/F_i^{FOV}} \quad \text{(Equation S5)}$$

where F_i^{GFP}/F_i^{FOV} is the fraction of the measured signal that effectively comes from GFP.

The entire PBR algorithm was performed separately in the distinct ROIs. Of note, in some samples with very dim GFP cytosolic signal we observed a deviation, with computed background lower than measured background. This is due to the PBR constraint that both GFP and BG corrections at each pixel have to be positive, therefore when the measured signal is weak the algorithm does not detect sufficient background to remove and thus overestimates the signal. Data showing such deviations was not included in any further analysis. Finally, the intensity F_i^{GFP} and brightness e_i^{GFP} maps were averaged separately in each ROI of each detected cell to yield protein concentration and stoichiometries states at the single cell/compartment level following Equations 3 and S2, respectively.

To estimate the accuracy of the data processing and PBR algorithm, we used the 1-photon system to acquire a set of 8 FOVs from untagged GFP-negative cells. These FOVs were split into 2 groups of 4, one of which was processed as if it was GFP-positive while the other group was used as untagged control FOVs. Four different combinations of pseudo-positive cells were evaluated, among which 3 yielded a significant deviation between measured and removed background (i.e., signal below the "detection threshold", as should be expected in the absence of GFP). However, one combination gave a better overlap between measured and removed background (though not perfect) and yielded an artefactual GFP concentration of 3-4 nM. We concluded from this analysis that the typical variability of background auto-fluorescence distribution over four FOVs is less than 3-4 nM. Then, variability in background-removal can affect measured concentrations only by 3-4 nM. Auto-fluorescent background was significantly reduced under the 2-photon system and therefore we estimated variability and uncertainty arising from background-removal to about 1nM. For this reason, Cln1- and Cln2-GFP fusions were only measured on the 2-photon system.

Data analysis was performed in the MATLAB (The Mathworks) environment with the MATLAB Image Processing Toolbox. The automated procedure, including single cell/nucleus masking, extracts the protein fusion fluorescence signal with a custom pixel-based probabilistic auto-fluorescence background subtraction algorithm, computes the monomeric GFP brightness, e_{GFP} from sN&B imaging of the free GFP strain and uses this value and the excitation volume V_{eff} to compute absolute protein concentrations from protein fusion average intensity using Equation 3. The cell size-independent yeast auto-fluorescence was deconvolved from the average intensity, $\langle F \rangle_{PF}$ (Figures S9 and S10).

Accuracy, Precision and Limits of sN&B

Following Equation 3 in the main text, the uncertainty in the values of the absolute concentrations of GFP fusion proteins in live yeast cells arises from uncertainty in three values, $\langle F \rangle_{PF}$, e_{GFP} and V_{eff} (Figures S1–S3). The GFP brightness value is well-determined from hundreds of thousands of pixels from 30-100 cells from multiple FOVs, such that the standard error on the mean of the distribution of single-cell e_{GFP} values resulting from this procedure (performed daily) is $\leq$2% (Figure S2C). The e_{GFP} calibration, performed in live yeast cells under identical growth and imaging conditions as for the strains expressing the fluorescent protein fusions, takes into account optical effects due to heterogeneities of the yeast cytoplasm or any difference in GFP quantum yield in the intracellular environment. We ascertained by induction of expression at various galactose concentrations that the GFP brightness was protein concentration independent from $\sim$10 nM to $\sim$1 μM, and hence that the GFP was indeed monomeric over this concentration range.

The accurate determination of the effective volume, V_{eff}, is also crucial. We estimate at less than 2% the uncertainty in the fluorescein concentration, because the OD is taken at high concentration where accuracy and precision are very good. Then the dilution is measured using fluorescence (which is more accurate than absorption at low concentrations) to verify the dilution factor. Given the hundreds of thousands of pixels used to determine V_{eff}, the estimated error is <2%.

The value of the effective volume cannot be determined *in cellulo*, as this would require the presence *in cellulo* of a fluorophore of known concentration. However, sample preparation protocols provide us with cell monolayers, in which the refraction index changes only moderately despite the presence of organelles. We tested how moderate variations of the refraction index affect the effective volume by determining values in solutions with variable glycerol concentrations, and found no detectable distortion of the excitation volume. We concluded that tiny cell compartments would have an insignificant effect on V_{eff}. In addition, since e_{GFP} is sensitive to distortions in V_{eff}, a strong effect of optical inhomogeneities due to organelles and other cellular compartments would increase the intracellular variability in e_{GFP} values, which, to the contrary, were found to be highly spatially homogeneous (Figures S2A and S2B). Homogeneous GFP brightness in live yeast cells indicated that the V_{eff} was not significantly altered by optical distortions due to intracellular structures such as membranes, organelles or large macromolecular complexes. Since the fluorescence lifetime of GFP was the same for free GFP and the various GFP protein fusions (Figure S5), the brightness per monomer was also equivalent. These observations demonstrated that the molecular brightness of free GFP, determined in live cells under the same conditions as the GFP protein fusions, was an accurate and reliable internal calibration parameter.

Since our calibration parameters, e_{GFP} and V_{eff}, were determined with high accuracy and precision, (Figures S2 and S3), as confirmed by the high reproducibility between experiments (Figures S6 and S7), the major source of inaccuracy in nuclear

concentrations of the fluorescent Start protein fusions arose from imperfect average intensity, $\langle F \rangle_{PF}$, measurements for the protein fusions. Inaccuracies arose from three sources: the z-focus of the nucleus, photo-bleaching during the 50 sN&B frames, and the contribution of yeast auto-fluorescence. To limit the uncertainty in perfect focus, we measured 3 z-positions separated by 500 nm (700 nm for 1-photon experiments) for each FOV and observed a typical small (<10%–15%) difference in $\langle F \rangle$ between the 2 z-positions showing the best signal for each nucleus, the third plane being often significantly out of focus ($\langle F \rangle$, damped by >40%). Thus, we estimated the average under-estimation of the intensity at ~15%/2=7.5 %. This uncertainty in z-focusing also represents the only measurement-dependent contribution to differences in measured intensity between nuclei of different cells, and at 7.5% is ~ 3-fold lower than the measured cell-to-cell variation. This demonstrates significant biological noise in the individual cellular concentrations of each protein fusion. Acquisitions of more planes spaced more closely along the z-direction did not improve the measurements or analysis. In contrast, for the cytoplasm, the z-focus position was not crucial.

Photo-bleaching is an unavoidable photochemical process that occurs regardless of the specific microscopy approach used (Shaner, 2014; Ettinger and Wittmann, 2015). To mitigate photo-bleaching effects, we used imaging parameters (i.e., laser power at the sample) and pixel dwell-time, such that photo-bleaching was at most ~10% over the 50 frames of the sN&B measurements (Figure S2D). Because the bleaching we observed was linear, this resulted in an underestimation of the average intensity over all frames of 5% (Figure S2D). Comparison of protein concentrations for the same fusion in two different conditions such as glycerol and glucose involved much less uncertainty in the relative values since the excitation volume and the e_{GFP} values were the same (i.e., these did not change with growth conditions).

A distinct advantage of sN&B over other particle counting approaches such as point or scanning FCS, lies in the time scale of acquisition (Figure S1A). Since the frame time in sN&B is 2-3 s, intensity fluctuations are observed, even for very slowly diffusing molecules, such as proteins that interact with DNA and dissociate stochastically on the ~100 ms to 1 s time scale. Note that on the line-time scale of sN&B (10-40 ms), these DNA-bound proteins are mostly immobile (Figures S4A–S4H). However, the fact that we measure finite, non-zero values of GFP fusion protein molecular brightness on the 2-3 s frame time shows that Start transcription factors actually move on the requisite 2-3 s time scale (Digman et al., 2008). This long time scale has several advantages over point FCS. First, since the beam is rapidly raster scanned it does not remain at a given pixel very long and thus photo-bleaching is greatly diminished. The raw molecular brightness value, B, of immobile particles is uniquely due to shot noise and is equal to 1, while true brightness, e, is equal to 0. Since all the brightness values measured for the protein fusions were $\geq e_{GFP}$, we conclude that the intracellular dynamics of the proteins are fast on the frame time of the sN&B measurements (~2.5 s). Moreover, for concentration determinations, neither the brightness values nor the number values of the GFP fusion proteins were used. Rather, the molecular brightness of free, cytosolic monomeric GFP was used with the average GFP fusion protein intensity, $\langle F \rangle$, as an internal calibration factor as per Equation 3 in the main text. Relatively fast diffusion of free GFP in the cytosol (5-10μm^2/s) ensured the reliability of its brightness value, and therefore the reliability of the GFP fusion protein concentration determination method. Of note, the Gfpmut3 variant used here matures in ~6 min *in vivo* (Megerle et al., 2008) and is monomeric (Cormack et al., 1996), thereby ensuring maximal accuracy in protein fusion concentration and stoichiometry values. Finally, in sN&B, while the molecules must move on the frame time scale, the cells and the nuclei must remain immobile. Cells were effectively immobilized on agarose pads (Figure 1D). However, occasionally, nuclei inside cells moved from frame to frame during an sN&B acquisition. When this occurred, the brightness maps exhibited very high values around the edges of these moving nuclei (Figure S4I), and as such were easily detected and eliminated from the analyses.

Overall then, we estimated the average uncertainty in sN&B determinations of GFP protein fusion concentrations in single cells to be $\leq$12% (Figure S1B). In addition, we note that imperfections in the discrimination of the fluorescent signal above the auto-fluorescence background yielded a lower limit of 1 nM using the 2-photon microscope and 3-4 nM using the confocal microscope. In a nucleus of 3-4fL, a concentration of 1 nM corresponds to 2 molecules.

Mathematical Modeling

A common approach to mathematically model biochemical pathways is to use ordinary-differential equations (ODEs) to represent protein association/dissociations in complexes, import and export from cellular compartments and enzyme activities. Parameters of such ODE-based models are reaction rates, sometimes independent of concentrations, but often not (for instance, complex formation follows mass-action kinetics and the larger the concentrations of complex components, the higher the complex formation rates). However, microscopic biochemical processes on the time scales of microseconds to seconds are generally very fast compared to cell growth processes that take several tens of minutes to hours. Therefore, the biochemical network reaches equilibrium before the cell grows again. Based on this rapid equilibrium, we opted to solve the coupled equations (Figure 6A) in the steady state to find the critical size at Start. The model comprises: 1) an SBF/MBF binding module, resolution of which yields the concentration of DNA-bound and DNA-free SBF/MBF complexes and the fraction of SBF- and MBF- bound G1/S promoter DNA in the cell nucleus as a function of cell size, and 2) a phosphorylation module, which integrates the solution of the first module to predict the size at which the Whi5-Swi6 inhibitory interaction is abrogated and Start is triggered (Figure 6A).

SBF/MBF Binding Module

Module Hypothesis. Our sN&B experiments revealed that nuclear Mbp1 and Swi6 concentrations were largely size-independent in G1 phase cells whereas the Swi4 concentration almost doubles between early G1 (50-60 nM in 10-14 fL cells) and late G1 phase (100-120 nM in 30-35 fL cells). As cells grow and progress through G1 phase, the number of target promoters remains constant ($\approx$200), yielding an effective dilution of target promoters from 166 nM in an early G1 nucleus to 66 nM in a late G1 nucleus, assuming

a karyoplasmic ratio of 1/7 (Jorgensen et al., 2007). Distinct structural domains of Swi4 and Mbp1 mediate their interactions with DNA and with Swi6. Hence, DNA binding was assumed to be independent of Swi6 binding for both Swi4 and Mbp1 (Siegmund and Nasmyth, 1996; Taylor et al., 2000). In other words, we assumed that interaction K_d values for the transcription factors (TFs = Swi4 or Mbp1) with DNA are unaffected by Swi6 binding, and vice-versa. In addition, our brightness data revealed that all measured Start proteins were predominantly dimeric. Thus, we reduced the model complexity by neglecting the equilibrium concentrations of protein complexes formed with monomer TFs and/or Swi6.

Module Equations. The SBF/MBF binding module reduces to 8 equilibrium reactions (with effective dissociation constants K_d that originate from the integration of monomeric Start factors into dimeric/tetrameric complexes, see Figure 6A), complemented with 4 standard conservation laws for the total concentration of each protein individually (and the total amount of promoter DNA):

$$
\begin{aligned}
&2\,TF + DNA \quad \leftrightarrows \quad DNA_{s,m} \quad , K_d = K_{s,m1}^2 \\
&2\,TF + 2\,Swi6 \quad \leftrightarrows \quad S(M)BF \quad , K_d = \frac{K_{s,m2}^4 K_{s,m3}}{K_{s,m1}^2} \\
&DNA_{s,m} + 2\,Swi6 \quad \leftrightarrows \quad S(M)BF^* \quad , K_d = \frac{K_{s,m2}^4 K_{s,m3}^2}{K_{s,m1}^4} \\
&S(M)BF + DNA \quad \leftrightarrows \quad S(M)BF^* \quad , K_d = K_{s,m3} \\
&[DNA] + [DNA_s] + [DNA_m] + [SBF^*] + [MBF^*] \quad = [DNA]_{tot} \\
&[Swi6] + 2 * [SBF] + 2 * [MBF] + 2 * [SBF^*] + 2 * [MBF^*] = [Swi6]_{tot} \\
&[Swi4] + 2 * [DNA_s] + 2 * [SBF] + 2 * [SBF^*] \quad = [Swi4]_{tot} \\
&[Mbp1] + 2 * [DNA_m] + 2 * [MBF] + 2 * [MBF^*] \quad = [Mbp1]_{tot}
\end{aligned}
\qquad \text{(Equation S6)}
$$

where *TF* can be either Swi4 or Mbp1, *DNA* and $DNA_{s,m}$ represent a TF-free and TF dimer-bound target promoter respectively, *S* (*M*) *BF* and *S* (*M*) *BF** are fully formed DNA-free and DNA-bound TF dimer-Swi6 dimer SBF and MBF complexes, and the microscopic dissociation constants $K_{s,m1}$, $K_{s,m2}$, and $K_{s,m3}$ respectively characterize monomer TF-DNA, monomer TF-Swi6 and dimer TF-DNA binding, with s and m lowercase standing for Swi4 and Mbp1, respectively. We chose to express protein-protein and protein-DNA affinities in terms of monomeric equilibrium constants since available *in vitro* measurements of dissociation constants mostly involve monomers in solution (Baetz and Andrews, 1999). The effective dissociation constants in Equation S6 were inferred from the study of the microscopic monomer-binding reactions required to build full SBF/MBF complexes. It is noteworthy that the dissociation constant of *S* (*M*) *BF* is not the microscopic TF/monomeric-Swi6 constant but an effective dimer-TF/dimer-Swi6 dissociation constant that involves multiple interactions:

$$
K_{s,m2eff} = \left(\frac{K_{s,m2}^4 K_{s,m3}}{K_{s,m1}^2} \right)^{1/3} . \qquad \text{(Equation S7)}
$$

The study of the conversion from monomeric to dimeric species also yielded conditions on the order of magnitude of microscopic K_d's under which the concentrations of complexes encompassing monomer TF/Swi6 can be reasonably neglected:

$$
\begin{aligned}
&K_{s,m1} < K_{s,m2} \text{ or} \\
&K_{s,m1} > K_{s,m2} \text{ and } \frac{K_{s,m3}}{K_{s,m2}} > \left(\frac{K_{s,m1}}{K_{s,m2}} \right)^2
\end{aligned}
\qquad \text{(Equation S8)}
$$

Parameter Estimations. While our sN&B measurements constrained the total concentrations of all factors (Figures 2 and 4), dissociation constants could not be estimated directly from our data. However, previous *in vitro* studies have estimated TF-DNA interactions to be in the 10-40 nM range (Deleeuw et al., 2008; Eriksson et al., 2011) and given the low protein concentrations measured, the TF-Swi6 interaction affinities must be in the same range or even higher. In addition, while it is still possible that effective Swi6-driven TF dimerization hides DNA-binding sites on both TF monomers and reduces the affinity of the full complex to DNA compared to monomer TF, it is likely that the multiplicity of DNA binding domains on full (dimer of dimer) SBF/MBF facilitates the interaction: $K_{s,m1} > K_{s,m3}$. In support of this view, in the absence of Swi6, Swi4 and Mbp1 bind their target sequences *in vitro* with lower affinity K_d >200 nM in a 1:1 stoichiometry (Taylor et al., 2000) and Swi4 binding to DNA is strongly reduced *in vivo* in G1 (Harrington and Andrews, 1996). Note that $K_{s,m1} > K_{s,m3}$ ensures that the conditions for neglecting monomeric species in complexes (Equation S8) are automatically satisfied. Accordingly, unless otherwise specified, we used the following default values: $K_{s1} = K_{m1} = 100\ nM$, $K_{s3} = K_{m3} = 20\ nM$, $K_{s2} = 20\ nM < K_{m2} = 50\ nM$. A thorough analysis of the parameter space is provided (Figures S17A–S17D).

Resolution Techniques. The algebraic equation system was solved numerically using in-house MATLAB scripts based on the MATLAB *fsolve* built-in function. For a given set of total protein concentrations (as measured by sN&B, with $[Swi4]_{tot}$ being a proxy for cell size) and microscopic K_d's ($K_{s,m1,2,3}$), the program computes the concentrations of all dimeric/tetrameric complexes, and

importantly, the fractions of SBF- and MBF-bound G1/S promoters. Despite involving rational fractions of 4th degree polynomials the system of equations presents no singularity. Thus, the solution of this chemical equilibrium is unique (Smith and Missen, 1982).

Phosphorylation Module

Module Hypothesis. The transcription burst at Start relies primarily on SBF and to a lesser extent MBF (Iyer et al., 2001; Simon et al., 2001). Our sN&B data show that total Swi4 concentration increases 2-fold throughout G1 phase. However, the output for the SBF/MBF binding module reveals that, even though most SBF is bound to DNA throughout G1 phase consistent with published observations (Harrington and Andrews, 1996), this significant increase only leads to a shallow peak in the concentration of DNA-bound SBF at intermediate size, resulting from an optimum in DNA-SBF binding efficiency, while Swi4 concentration increases and DNA promoter concentration decreases. This makes the concentration of DNA-bound SBF (not to be confused with the fraction of DNA promoters bound by SBF) unlikely to be a key metric controlling Start trigger.

In vivo, DNA-bound SBF is repressed in G1 phase WT cells owing to Whi5-mediated inhibition of SBF via the Swi6-Whi5 interaction. As the Whi5-binding and Swi4/Mbp1-binding sites on Swi6 are distinct (Siegmund and Nasmyth, 1996; Travesa et al., 2013), we assumed no energetic cooperativity between Swi6 binding to Whi5 and Swi4 (or Mbp1), thereby decoupling the SBF/MBF binding module and the phosphorylation module. In late G1, disruption of the Whi5-Swi6 inhibitory interaction requires the phosphorylation of a minimal number of sites on the complex, and is self-amplified by the active SBF/MBF-mediated transcription of *CLN1/2* that in turn increases overall Cdc28-phosphorylation activity (Wagner et al., 2009; Skotheim et al., 2008). There is currently no consensus on how, quantitatively, the relief of SBF inhibition together with, possibly, MBF activity, affects G1-cyclin levels and feeds back to the disruption of Whi5-Swi6 interaction. The resolution of the SBF/MBF binding module showed that, unlike the concentration of DNA-bound SBF, the fraction of SBF/MBF-bound G1/S promoters substantially increases with growth. Given that the *CLN1-2* promoters both contain SCB and/or MCB consensus sequences, and are ranked among the top 30%–40% of preferred SBF/MBF targets in microarray experiments (Iyer et al., 2001; Simon et al., 2001), we hypothesized that a minimal level of G1/S promoter saturation was required before *CLN1-2* expression was activated. On the other hand, G1 cyclin turnover rates are significantly faster than growth (Tyers et al., 1992, 1993; Schneider et al., 1998), therefore at shorter biochemical time scales phosphorylation activity was assumed to mirror cell growth-dependent changes in *CLN1/2* promoter activity, related to the fraction of active promoters (see below). In addition, our sN&B data on Cln1/2-GFP concentrations shows that MBF contributes to G1 cyclin expression, even though this contribution is hindered by SBF when Swi4/Mbp1 concentrations are comparable, consistent with the expectation that SBF binds more readily to *CLN1/2* promoters than MBF (Harris et al., 2013).

Module Equations. According to the multi-site phosphorylation mechanism described above, while the binding rate of the Whi5-Swi6 complex can be considered as phosphorylation-independent, only complexes that have been phosphorylated on enough sites on both Whi5 and Swi6 (total sites denoted *M*) can dissociate. As a consequence, the effective "off" rate is proportional to the fraction of complexes that have reached this minimal phosphorylation state, and the effective Whi5-Swi6 dissociation constant, K_{ws}, behaves as:

$$K_{ws} = K_0 \frac{[M - phosphorylated\ Whi5 - Swi6\ complexes]}{[all\ Whi5 - Swi6\ complexes]} \quad \text{(Equation S9)}$$

where K_0 is a constant that must be large enough so that, when all Whi5-Swi6 complexes are M-phosphorylated, the complex is effectively disrupted (thus, $K_0 > [Whi5]_{tot}$, $[Swi6]_{tot}$). While deciphering the full dynamics and equilibrium properties of the different Whi5-Swi6 phosphorylated species is beyond the scope of this paper, simple arguments capture the essentials of K_{ws} scaling as a function of effective phosphorylation activity. Indeed, if C_n denotes the concentration of n-phosphorylated Whi5-Swi6 complexes, a simple multi-site phosphorylation dynamics model, in which each site is phosphorylated/dephosphorylated at the same rates k_p and k_d respectively, independently of other sites yields:

$$\frac{\partial C_n}{\partial t} = k_p C_{n-1} + k_d C_{n+1} - (k_p + k_d) C_n \quad \text{(Equation S10)}$$

and in the steady state ($\frac{\partial C_n}{\partial t} = 0$), the vector $\{C_n\}$ is the eigenvector of a tridiagonal matrix involving the renormalized phosphorylation activity $p = k_p/k_d$ with eigenvalue 0. Such tridiagonal matrices are well studied (Kouachi, 2006) and yield $C_n \sim p^n$, that is, *n* individual phosphorylation events must occur to generate the n-phosphorylated complex. Thus, the effective Whi5-Swi6 dissociation constant scales as.

$$K_{ws} = K_0 \frac{p^M * k(p)}{1 + p + p^2 + \ldots + p^M * k(p)} \quad \text{(Equation S11)}$$

where $k(p) = 1 + p + p^2 + \ldots$ integrates the contributions of all the species phosphorylated at least *M* times. Without loss of generality, we used $k(p) = 1$, leading to Equation 4 of the main text. This simplification does not alter the $p \ll 1$ and $p \gg 1$ asymptotic regimes where K_{ws} vanishes as $K_0\, p^M \ll K_0$ and saturates to K_0 respectively. The intermediate regime exhibited a sigmoidal function of the phosphorylation activity, *p*. We performed a full resolution of the equilibrium binding of Whi5-Swi6 phosphorylated species in the presence of Whi5 nucleo-cytoplasmic shuttling (not shown). This work confirmed the sigmoid-like dependence of the Whi5-Swi6 effective dissociation constant K_{ws} on the effective phosphorylation activity $p = k_p/k_d$.

Next, we assumed that the phosphorylation activity is a linear function of the fractions of active, Whi5-free SBF- and MBF-bound DNA target promoters (Equation S12):

$$p = \frac{f_{SBF} * f_{Whi5-free}}{\alpha} + \frac{f_{MBF}}{\beta} \quad \text{(Equation S12)}$$

where $f_{S(M)BF} = \frac{[S(M)BF^*]}{[DNA]_{tot}}$ are the fractions of SBF- and MBF-bound promoters, and $f_{Whi5-free}$ is the fraction of SBF complexes liberated from Whi5 inhibition, supposed to be identical for DNA-free and DNA-bound SBF given the independence of DNA- and Whi5-binding on SBF, mediated by distinct protein domains. The parameters α and β are detailed below. Note that taking into account Cln3 phosphorylation activity towards Whi5-SBF would add a (small) K_{ws}-independent positive contribution to the phosphorylation activity that would shift the purple sigmoid plots to the left on Figure 6D, thus shifting the appearance of a large K_{ws} solution to smaller size. In agreement with the extreme small size phenotype of cells overexpressing *CLN3* or *CLN3-1* (Nash et al., 1988; Tyers et al., 1992), a significant increase for this contribution would permit the high K_{ws} solution even at small sizes.

While f_{MBF} and f_{SBF} are completely determined as a function of cell size via resolution of the SBF/MBF binding module, $f_{Whi5-free}$ is determined straightforwardly by the resolution of the following steady-state mass action equations, written in the dimer form without distinction of status with respect to DNA binding:

$$\begin{array}{l} 2\,Whi5 + FreeSBF \quad \leftrightarrows \quad InhibitedSBF, K_d = K_{ws}^2 \\ [Whi5] + 2 * [InhibitedSBF] \quad = \quad [Whi5]_{tot} \\ [FreeSBF] + [InhibitedSBF] = [SBF] + [SBF^*] \end{array} \quad \text{(Equation S13)}$$

from which we obtain:

$$f_{Whi5-free} = \frac{FreeSBF}{[SBF] + [SBF^*]} = \frac{1}{1 + \frac{[Whi5]^2}{K_{ws}^2}} \quad \text{(Equation S14)}$$

where the concentration [Whi5] of Whi5 not bound by SBF solves the conservation law:

$$[Whi5] + 2 * \frac{\frac{[Whi5]^2}{K_{ws}^2}}{1 + \frac{[Whi5]^2}{K_{ws}^2}} * ([SBF] + [SBF^*]) = [Whi5]_{tot} \quad \text{(Equation S15)}$$

and where the SBF/MBF binding module outputs, [*SBF*], [*SBF**], depend on cell size but not on K_{ws} and/or phosphorylation, and $[Whi5]_{tot}$ is the size-independent nuclear Whi5 concentration determined experimentally by sN&B.

Parameters. The phosphorylation module adds 3 new parameters to the full model. *In vivo,* the Whi5-Swi6 interaction is disrupted concomitantly with the G1/S phosphorylation burst, where the phosphorylation rate exceeds the de-phosphorylation rate ($p \gg 1$). In this limit, $K_{ws} = K_0$ which therefore must be larger than $[Whi5]_{tot}$, $[Swi6]_{tot}$ otherwise the complex would not dissociate. Unless otherwise specified, we chose $K_0 = 1\ \mu M$. In addition, the transition between the low and high K_{ws} regimes occurs in the intermediate phosphorylation range where $p \sim 1$, achieved when the fraction of TF-bound promoters is $\sim\alpha$, β for SBF and MBF respectively. Our sN&B data indicate that SBF plays a greater role in *CLN1/2* expression, therefore we chose $\alpha < \beta$. According to microarray data, which ranked *CLN1/2* promoters among the top 30% of preferred SBF/MBF-dependent promoters (Iyer et al., 2001; Simon et al., 2001), we estimated these critical fractions at about 30%. Hence, we chose α = 0.30, β = 0.6. The average critical size for WT (28 fL) and *mbp1Δ* (32 fL) in glucose were used to adjust model parameters α and β to these values. Interestingly, good quantitative fit was obtained for $\beta = 2^*\alpha$, *e.g.* for a two-fold lower MBF activity (compared to SBF) towards *CLN1/2* expression, in agreement with G1 cyclin concentration being 2-fold lower in the absence of Swi4 (Figure 5).

Critical Cell Size at Start

General Remarks on Parameterization and Cell Size. The output of the phosphorylation module is an implicit fixed-point problem for K_{ws} (Equations S11 and S12), where the coefficients that set the relationship between phosphorylation activity and K_{ws}, i.e., outputs of the SBF/MBF binding module, are cell-size dependent. In short, if $K_{ws} \ll K_o$, regardless of cell size we have $f_{Whi5-free} \ll 1$ and p is limited to MBF transcription. Thus, the phosphorylation activity does not peak ($p < 1$), the right-hand side of Equation S11 is small ($p^M \ll 1$) and the fixed-point problem has always a solution $K_{ws} \ll K_o$, which corresponds to strong Whi5-Swi6 inhibition (pre-Start). If $K_{ws} \sim K_0 > [Whi5]_{tot}$, $f_{Whi5-free} \sim 1$ and p increases: the fixed-point equation might also be solved for larger $K_{ws} \sim K_0$. For fixed set of parameters, depending on cell size, the fixed-point equation can have 1 or 3 solutions (see Figure 6D). For small cells, the only solution of the complete model is $K_{ws} \to 0$, Whi5-Swi6 interaction is strong and Whi5 (in excess) saturates and inhibits SBF, and G1/S transition is "off" (pre-Start). For larger cells, $K_{ws} \sim K_0 > [Whi5]_{tot}$ is possible and Whi5-Swi6 interaction is much weaker, Whi5 is released from SBF, and the G1/S transition is "on". Thus, the system operates a size-dependent switch-like transition at a critical size, below which $K_{ws} \ll [Whi5]_{tot}$, $[Swi6]_{tot}$ is the only possible cellular state and above which $K_{ws} \gg [Whi5]_{tot}$, $[Swi6]_{tot}$ becomes possible. In this regime a tiny increment of cell size leads to a huge increment in K_{ws}. In our model, this defines the critical size at Start (Figure 6E). Note that our static model does not discuss how this transition happens dynamically. Depending on model parameters, we identified regimes where K_{ws} varies smoothly with cell size, with no such discontinuity. Specifically, we observed 4 different classes of model responses (see Figure S17): constitutive pre-Start ($K_{ws} \ll$ 120nM at all sizes), constitutive post-Start ($K_{ws} \gg$ 120nM at all sizes), smooth G1/S transition (K_{ws} varies smoothly with cell size), and switch-like G1/S transition

(described above, Figure 6E). The different classes of model responses cluster in particular regions of the parameter space, determined by the effective dimer dissociation constants of the SBF/MBF binding module of the full model. In the situation of a smooth Start transition where a tiny increment in cell size results in a tiny increment in K_{ws}, the critical size at Start was defined as the size above which $K_{ws} > [Whi5]_{tot} = 120\ nM$, corresponding to increased phosphorylation.

Resolution Techniques. The fixed-point problem was solved numerically using in house MATLAB scripts. First, for any set of parameters, we sampled cell size range (typically 10-50 fL sampled to 200 cell size points, extended for some conditions with large size phenotypes). Next, for each individual cell size value, we computed the total Swi4 concentration according to our sN&B data. Other total protein concentrations were size-independent. We next solved the SBF/MBF module, anchoring coefficients of the phosphorylation module fixed point equation system (main text Equations 4, 5, S11, S12, S13, S14, and S15). Then, the largest solution K_{ws}^{**} (see Figure 6D) was computed iteratively using the following iterative algorithm:

- set K_{ws} to maximal value K_0
- calculate $f_{Whi5-free}$ (K_{ws}, *size*) using the analytical solution of Equation S15, and infer the phosphorylation activity p from Equation S12.
- update K_{ws} using the sigmoid-like expression Equation S11.
- reiterate from step 2 until the relative change in K_{ws} is less than 0.1% between 2 iterations.
- go to the next cell size value.

This algorithm was found to be efficient and stable in solving the fixed point problem. Finally, we represented K_{ws}^{**} as a function of cell size (Figure 6E) and computed the size at which $K_{ws}^{**} > [Whi5]_{tot} = 120\ nM$. Of note, given the switch-like behavior of the transition under most parameter regimes, the particular choice of the K_{ws}^{**} threshold (120nM) had little (if any) effect on the critical size.

DATA AND SOFTWARE AVAILABILITY

All raw sN&B and confocal images (in .bin or .tiff format) are stored on dedicated file servers and are available upon request. The MATLAB software used in sN&B analysis and for the mathematical model of Start is also available upon request.